Nanoscale Advances

ROYAL SOCIETY OF CHEMISTRY

REVIEW

View Article Online
View Journal | View Issue

Cite this: *Nanoscale Adv.*, 2024, **6**, 367

Future prospects of MXenes: synthesis, functionalization, properties, and application in field effect transistors

Maisha Rahman and Muhammad Shamim Al Mamun *

Received 11th October 2023
Accepted 11th December 2023

DOI: 10.1039/d3na00874f

rsc.li/nanoscale-advances

MXenes are a family of two-dimensional (2D) materials that have drawn a lot of interest recently because of their distinctive characteristics and possible uses in a variety of industries. This review emphasizes the bright future prospects of MXene materials in the realm of FETs. Their remarkable properties, coupled with their tunability and compatibility, position MXenes as promising candidates for the development of high-performance electronic devices. As research in this field continues to evolve, the potential of MXenes to drive innovation in electronics becomes increasingly evident, fostering excitement for their role in shaping the future of electronic technology. This paper presents a comprehensive overview of MXene materials, focusing on their synthesis methods, functionalization strategies, intrinsic properties, and their promising application in Field Effect Transistors (FETs).

Introduction

In recent years, the pursuit of novel materials with exceptional properties and versatile applications has driven scientific research and technological innovation.[1] Among these emerging materials, MXenes, a group of transition metal carbides and nitrides in two dimensions (2D), have emerged as a compelling class of materials with immense potential. The unique combination of properties exhibited by MXenes, such as high electrical conductivity, mechanical robustness, and tunable surface chemistry, has positioned them as a promising candidate for a wide range of applications, particularly in the realm of electronic devices.[1–4]

The typical configuration of MXenes, according to Zhu *et al.* and Hieu *et al.*, is $M_{n+1}X_nT_x$, where M, X, and T stand for a transition metal, carbon/nitrogen, and surface terminal functional groups like O, F, and OH, respectively.[5,6] According to Hieu *et al.* a considerable number of functional groups for gas detection in MXenes, are particularly sensitive at various temperatures. MXenes may disperse in a variety of polar solvents because of the oxygen and fluorine species present on their surface.[7,8]

MAX can be converted into MXenes using a variety of etching techniques. MAX phases are a large family of hexagonal layered ternary transition metal carbides, carbonitrides, and nitrides with more than 60 members. They have the chemical formula $M_{n+1}AX_n$, where M denotes an early transition metal (like Ti, V, Cr, Nb, *etc.*), A denotes a group A element (like Al, Si, Sn, In, *etc.*), X denotes carbon and/or nitrogen, and $n = 1$, 2, or 3.[9–11] The integer n is the number of active groups. Even though a large number of MXenes with varied compositions have been postulated, only a few of them have ever been created. Due to the diversity of MXene compositions, numerous MXenes with desired qualities can be created.[7,12,13]

The M–X layer is alternatively ordered with an A atomic layer thanks to a metallic link between A and M; however M–A bonds are weaker than M–X interactions.[14] For the synthesis of MXenes, the weakly bound and most reactive A layers are etched away by various procedures (*e.g.*, HF, LiF/HCl, and NH_4HF_2). Strong etchants, like Cl_2 gas, at above 200 °C bring in the etching of both the A and M atoms, to yield carbide derived carbons.[15] Similar to this, Ti_2AlC was etched with anhydrous hydrofluoric acid (HF) at 55 °C, which led to the production of Ti_2AlF_9, a novel ternary metal fluoride phase. Therefore, a systematic equilibrium between temperature and the activity of the etchant must be established in order to selectively etch the A element while maintaining the 2D nature of the $M_{n+1}X_n$ layers. Weakly bound stacks of $M_{n+1}X_nT_x$ comprising 2D sheets with greater lattice parameters along the *c*-axis than MAX-phases (Ti_2AlC has $c = 13.6$ A, whereas Ti_2C has $c = 15.04$ A) are produced by delamination.[13]

MXenes are typically investigated for a wide range of potential uses, including anodes in lithium-ion batteries, supercapacitors, and catalysis.[9,11,13] The Ti_3C_2–MoS_2 composite was used by Le *et al.* to develop a novel gas sensor based on the material's highly active surface sites, electrical conductivity, and wide surface area.[16] MXene–graphene field-effect transistor sensing of influenza virus and SARS-CoV2 is a study done by Li *et al.* in 2021.[17] The conductive carbide core of the MXenes' 2D material, which has a huge surface area and good thermal conductivity, has unique properties for sensor applications.[18] In

Chemistry Discipline, Khulna University, Khulna-9208, Bangladesh. E-mail: s.mamun@chem.ku.ac.bd

addition, the valence band maximum can be altered in accordance with the "d-band center theory"[19] to enhance the catalytic activity of various MXenes. By selecting the right transition metal, it is possible to change the electronic band filling and subsequently the location of the 3d or 4d-band. Furthermore, by optimizing various surface interactions with various termination species, the surface chemistry of MXenes can be altered.[20] MXene properties can be tuned to suit specific applications by introducing heteroatoms, adjusting surface chemistry, or integration with other materials to enhance their performance in various contexts.

This paper embarks on a comprehensive exploration of the future prospects of MXenes, with a particular focus on their synthesis methodologies, functionalization strategies, intrinsic properties, and their application in Field Effect Transistors (FETs). MXenes have garnered substantial attention from the scientific community due to their intriguing characteristics, and this review aims to provide a holistic understanding of their role in shaping the future of electronic technology.

The synthesis of MXenes is a pivotal aspect of this investigation, as it forms the foundation for their utilization in various applications. A critical examination of these synthesis routes, their scalability, and the resultant material properties sets the stage for understanding the potential and limitations of MXenes. Functionalization is another key facet of this exploration. It explores the means by which MXene properties can be tailored to suit specific applications. Understanding these functionalization strategies is crucial to unlocking the full potential of MXenes in electronic devices. The intrinsic properties of MXenes, such as their remarkable electrical conductivity, mechanical resilience, and large surface area, form the core of their appeal in electronic applications. These properties, thoroughly discussed in this review, underpin their use in FETs and other electronic devices. Lastly, this review explores the practical application of MXenes in field effect transistors. Recent advancements in MXene-based FETs are highlighted, showcasing their potential for high-speed electronics, flexible and transparent circuits, and sensor technologies. The compatibility of MXenes with conventional semiconductor processes, such as complementary metal-oxide–semiconductor (CMOS) technology, underscores their seamless integration into existing electronic platforms.

Synthesis of MXenes

Structurally MAX phases are layered hexagonal materials.[21] In the MAX phase, the M and X atoms are arranged in a hexagonal lattice as seen in Fig. 1, and the edges and the X atoms share the M octahedral cage at its center. The M_nX_{n-1} layer can be created by etching the atoms of A because when A is removed, the M_nX_{n-1} can still maintain a hexagonal lattice rather than a cubic one. The transition metal surfaces are terminated by OH, F/Cl, and O as the synthesis is carried out (F/Cl depends on the etching process). The MXene is a multilayered substance with a morphology that resembles vermiculite clay after the etching procedure. These multilayers are kept together by a combination of hydrogen and van der Waals bonds because of surface terminations.[22] By intercalating massive cations from organic base solutions such tetrabutylammonium hydroxide, choline hydroxide, and *n*-butylamine, wide-scale delamination of various MXenes was accomplished. This was done by taking advantage of the MXenes' negative surface charge and spontaneous cation intercalation. The hydrophilicity of MXenes and their ease of dispersion in water without the need of surfactants make processing them simpler.

The preparation methods are classified as follows.

Etching methods

HF etching. HF etching is the most effective process of removing the "A" layer from MAX. It was first proposed by Naguib *et al.* in 2011. HF etching is typically performed by adding MAX into the hydrofluoric acid solution and continuously stirring the solution, as shown in Fig. 1a. Then the resulting suspension must be washed several times with deionized water. When the black coloured supernatant is stable, even though after centrifuging upto 1 h, the sediment is dissolved in deionized water and kept under sonication for an hour.[24–27]

$$Ti_3AlC_2 + 3HF = AlF_3 + 3/2H_2 + Ti_3C_2 \quad (1)$$

$$Ti_3C_2 + 2H_2O = Ti_3C_2OH_2 + H_2 \quad (2)$$

$$Ti_3C_2 + 2HF = Ti_3C_2F_2 + H_2 \quad (3)$$

The etching time depends also on the M atom. The M atoms with a larger number of valence electrons require stronger etching. For example, Nb_2AlC requires three times longer stirring time than $Ti_3C_2T_x$.[28] Though etching of MXenes with HF produces a high yield, this process is hazardous due to the highly toxic and corrosive nature of HF. So, it is critical to follow safety measures during work with HF. This etching process produces H_2 gas as a byproduct; this gas is highly flammable and easily escapes to the surrounding environment.[29] Fig. 1b shows the SEM images of MXenes after HF treatment and Fig. 1c shows different types of MXene structures.

As the HF is highly corrosive and toxic, some following alternative methods are explored.

(i) Molten fluoride-based etching method: to overcome the above limitation with HF, LiF : NaF : KF = 29 : 12 : 59, weight ratio, a molten fluoride salt was developed by Urbankowski *et al.* as an etchant.[30] This procedure occurs under high temperatures. The etching process can be completed within 30 minutes, which is very effective. As this process needs a high temperature this can be a demerit of this process.

(ii) LiF/HCl method: as HF is hazardous, a new method is introduced to remove A from MAX, using LiF/HCl as the etchant. Li^+ ion continuously intercalates between the MXene layer and thus weakens the bonding between M and A and successively removes the A layer from MXenes.[27] This process also produces H_2 gas, which is flammable.[29]

(iii) MS-E-etching process (molten salt assisted electrochemical etching: fluorine-free): the methods discussed above have a harmful influence on the environment. This method can be

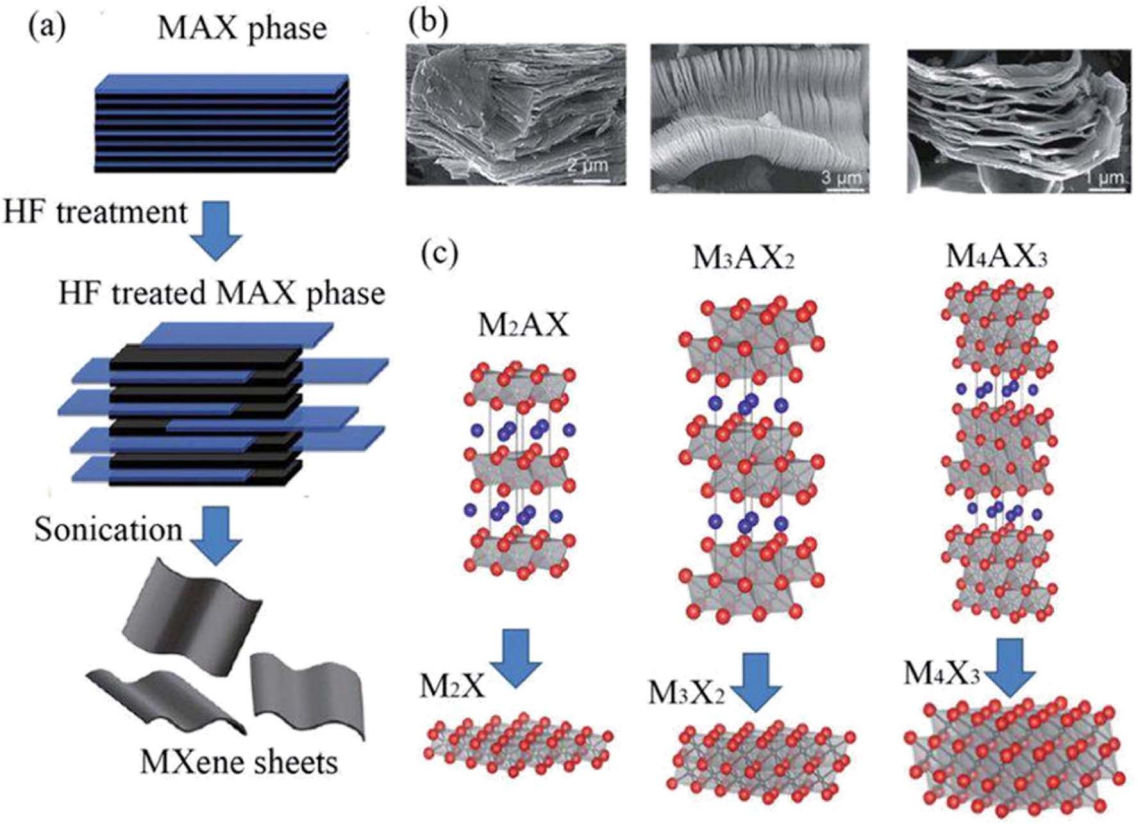

Fig. 1 (a) Three distinct MXene (non-terminated) structures were initially reported: M_2X, M_3X_2, and M_4X_3. (b) SEM pictures of Ti_2AlC, Ti_3AlC_2, and Ti_4AlC_3 (from right to left) after HF treatment. (c) Illustration of the synthesis of MXenes from MAX phases in a schematic form.

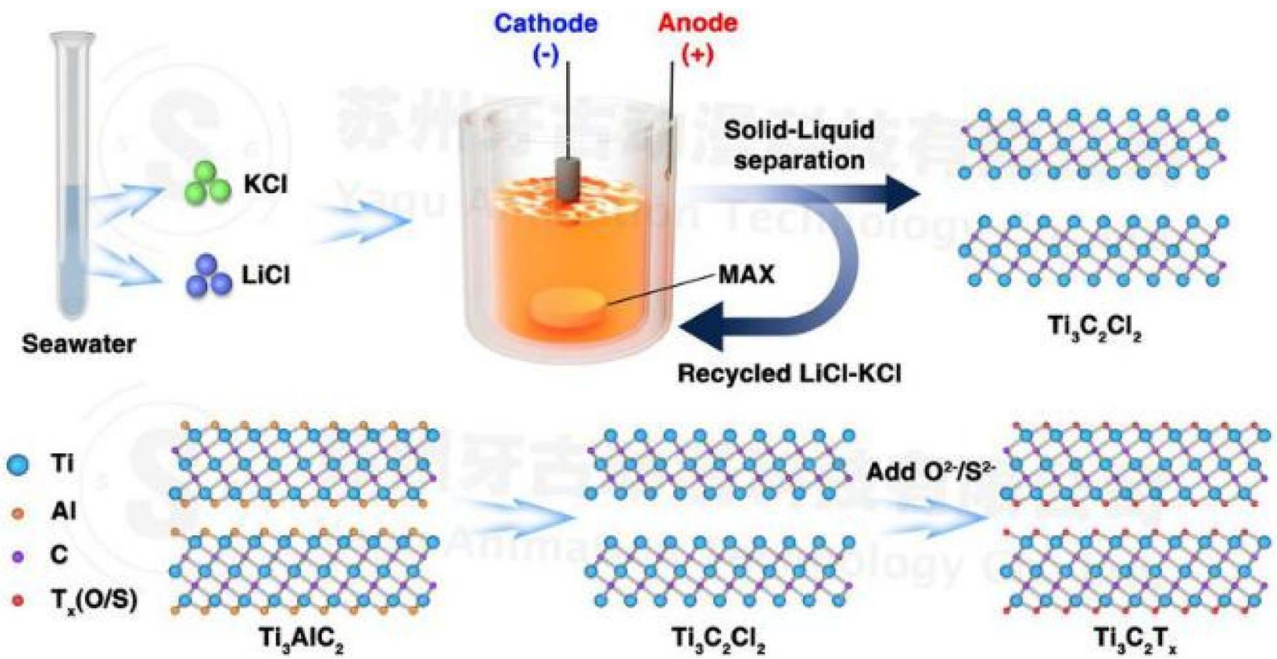

Fig. 2 Synthesis of MXenes through MS-E-etching from the MAX phase, followed by the controlled surface terminations facilitated by ample lithium and potassium resources found in salt lakes. Notably, the utilization of eutectic salts comprising LiCl and KCl, characterized by a low melting point, contributes to the controllability of the process (copyright 2021 John Wiley and Sons).[32]

easily accessible due to adequate lithium and potassium resources in salt-lakes and LiCl–KCl (1 : 1 wt%) salts at 450 °C. From Fig. 3 we can see that when a potential 2.0 volt is applied, $Ti_3C_2T_x$ releases electrons from its active sites and the Cl atom absorbs onto this active site, forming a strong $AlCl_3$ bond.[31] As the boiling point of $AlCl_3$ is 180 °C it can rapidly evaporate at 450 °C.[32] This process is environmentally friendly and the recovered salt after synthesis can be recycled and reused (Fig. 2).[33,34]

Etching methods are relatively simple and widely used. However, this process requires hazardous and toxic chemicals (*e.g.*, HF), and specialized safety precautions, which limit its use in MXene preparation.

Chemical vapor deposition

Alternative approaches to MXene synthesis, including bottom-up methods like chemical vapor deposition (CVD), have shown promising results.[35,36] For instance, in 2015, ultrathin 2D α-Mo_2C crystals, with thicknesses of only a few nanometers and lateral dimensions of up to 100 micrometers, were successfully produced through CVD. This process involved utilizing methane on a bilayer substrate composed of copper foil placed on a molybdenum foil.[35] This CVD technique has also been extended to create ultrathin WC and TaC crystals using other transition metals like W and Ta.[35] Notably, this method offers the advantage of generating MXenes with substantial lateral sizes and minimal defects, which greatly facilitates the investigation of their intrinsic properties. While the synthesis of MXene monolayers using this method has yet to be demonstrated, there is still room for further exploration and development of bottom-up synthesis approaches for MXenes. CVD offers precise control over MXene thickness and morphology. However, this process needs sophisticated instruments and skilled operators.

Synthesis of functionalized MXenes

Zr doped MXenes. With the help of magnetic stirring, $ZrOCl_2 \cdot 8H_2O$ (0.8 g, 2.5 mmol) was initially dissolved in 300 mL of $Ti_3C_2T_x$ aqueous dispersion (1.5 mg mL^{-1}) before being pH-adjusted with HCl to 1.0. The mixture was then given 1.0 g of AMP (50% solution), which was added dropwise, and refluxed for 12 hours at 100 °C. Centrifugation was used to separate the resulting Zr–MXene, which was then cleaned with deionized water before being dried for 48 hours at 50 °C under vacuum. About 91% of Zr–MXene was produced. Illustration of the synthesis process is shown in Fig. 3. In this study, a hybridized fire retardant (Zr–MXene) is described that has previously unheard-of levels of toughness, tensile strength, resistance to fatigue generation, and reduced flammability. This offers a viable method for producing polymeric nanocomposites made of multifunctional MXenes.[37]

Functionalization of MXenes by silylation

There is a need to improve MXenes' stability. Ji *et al.* demonstrated a straightforward silylation approach (shown in Fig. 4) for successfully stabilizing MXenes against spontaneous oxidation-induced structural breakdown and improving surface properties with variable hydrophilicity.[38] The MXene solution was centrifuged at 13 000 rpm for about 30 min. The sediment was then collected and dissolved in 95 percent pure ethanol. Hexadecyltrimethoxysilane, 3-aminopropyl triethoxysilane, and 1*H*,1*H*,2*H*,2*H*-perfluorodecyltriethoxysilane were all reacted with 200 L of MXenes in ethanol (total volume 2 mL) at various concentrations (0, 1, 5, 10, 20, 50, 100, 200, 500, and 1000 L). The samples were then each repeatedly rinsed with water and dissolved in 1 mL of water.

MXene nanosheet doped tin oxide. The freeze-dried MXene nanosheet (200 mg) was disseminated in the precursors of dodecyltrimethoxysilane and FOTS (10 wt% in 20 mL ethanol) under stirring for 24 hours, resulting in MXene–H and MXene–F, respectively. Following this reaction, the product was centrifuged numerous times at 6000 rpm for 10 minutes while being rinsed with DI water and ethanol. By freeze drying for 24 hours, the final functionalized MXene nanosheet was obtained.[39]

Cesium-doped MXene. CsCl (1 mg mL^{-1}) was dissolved in deionized water to create Cs–$Ti_3C_2T_x$, which was then sonicated in a bath for 10 minutes. Then, 10 mg of the freshly synthesized MXene was dissolved in 10 mL of CsCl solution, and the mixture was agitated for 30 minutes on a flask shaker. 10 mg of the as-produced MXene was dissolved in 10 mL of deionized water to create p-$Ti_3C_2T_x$. To prevent oxidation, the produced MXene dispersions were next centrifuged at 3500 rpm for 30 minutes before being bath sonicated for 10 min. The pellet at the bottom was redispersed in DMF at the same concentration after the

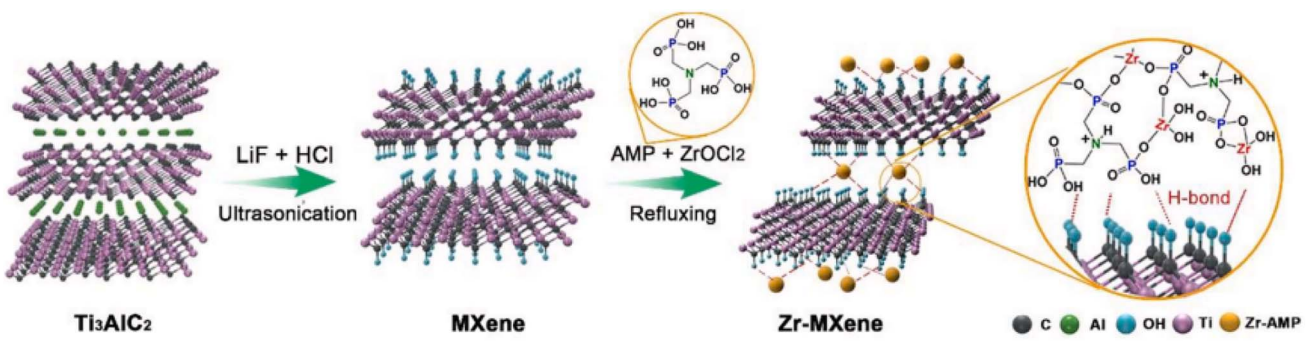

Fig. 3 Scheme for the Zr–MXene preparation.[37]

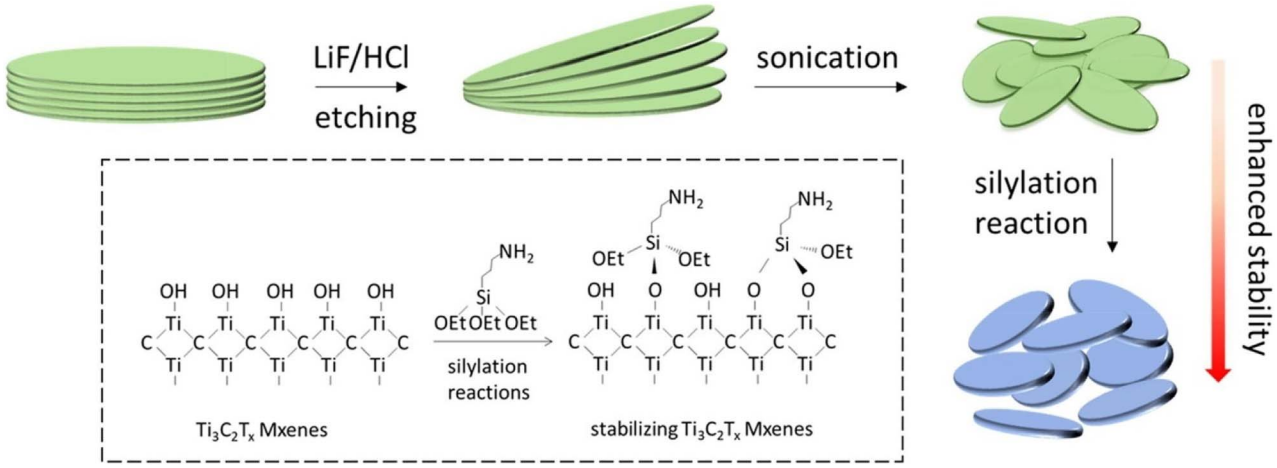

Fig. 4 Selective etching and sonication of MXenes with LiF/HCl (copyright 2019 Elsevier).

supernatant was discarded. To get rid of any remaining water, this step was repeated three times. After 5 minutes of sonication under Ar flow, all samples were processed. All dispersions were then chilled (4 °C) and degassed with Ar for 10 minutes before being used.[40]

MXenes can, therefore, be created in a variety of forms, including multilayer powders and inks made of delaminated flakes dissolved in water. These inks can then be printed, sprayed, pulled into fibers, or filtered into freestanding films. The etching technique, the intended application, the needed concentration, and the sonication step all play a significant role. Longer sonication times and stronger sonication forces will result in smaller flakes with more flaws and maybe different concentrations than non-sonicated samples. The technique of synthesis and the kind of intercalants employed to reduce the inter-layer contact between MXene sheets are two additional factors that affect the concentration of MXene sheets in solution. This section details the benefits and drawbacks of processing $Ti_3C_2T_x$. Ultrasonic is another method other than etching which reduced the etching time to 4 h to 24 h. In this method $Ti_3C_2T_x$ was slowly added to an etchant in a beaker, and then the beaker was placed into an ultrasonic homogenizer for 4 h[23] As there is a different etching process, different groups can be attached with M atoms and the characteristic of the surface of MXenes highly depends on their preparation method.[22]

Characterization

Several characterization techniques are commonly employed to analyze MXenes. Visual appearance is an important aspect of MXene characterization, as it provides qualitative information about the morphology, color, and texture of MXene materials. MXenes are a class of two-dimensional materials with unique properties, and their characterization is crucial for understanding their structure, properties, and potential applications. FTIR helps identify functional groups and chemical bonds present in MXenes. It is particularly useful for assessing surface modifications and chemical interactions.[41] UV-Vis spectroscopy plays a crucial role in MXene characterization by providing valuable information about their electronic structure, optical properties, concentration, stability, and chemical modifications.[42]

Accurately quantifying the ratio of oxygen groups (=O) to hydroxyl groups (–OH) on MXene surfaces presents a formidable challenge. Similarly, the quantitative analysis of fluorine termination (–F) is problematic due to the formation of fluoride by-products, such as AlF_3. The detection of light elements is generally challenging in analytical science because of their low atomic mass and compact electron clouds. Nuclear Magnetic Resonance (NMR) is a technique that probes atomic nuclei when there is a deviation from a spin number of 0. Hydrogen (H) and fluorine (F) are amenable to NMR analysis because they possess an odd number of neutrons. NMR experiments have provided insights into MXene surface chemistry, revealing that there are fewer –OH terminations compared to –F or –O terminations on the surface of $Ti_3C_2T_x$. Furthermore, these studies have demonstrated the high sensitivity of surface terminations to the specific synthesis methods employed.

Apart from these several characterization techniques are adopted for the MXene, which are illustrated in this section.

Raman spectroscopy. Peaks labeled 1, 2, 3, and 4 were visible in the Raman spectra of the carved $Ti_3C_2T_x$ MXene and the Ti_3AlC_2 starting material in the MAX phase. The broadening of the peaks in the MXene spectrum was associated with a decrease in order, and these peaks were linked to shear and longitudinal oscillations of Ti and the Al atoms.

Additionally, two broad peaks between 1000 and 1800 cm^{-1} were seen in Fig. 5, and these were identified as the D and G peaks of graphitic carbon. The increased laser power, which caused the creation of oxidized Ti_3C_2, may be to blame for the peak's high intensity at about 151 cm^{-1}. These findings, which are corroborated by several accounts in the literature, indicate that $Ti_3C_2T_x$ was successfully synthesized. The out-of-plane vibrations of the Ti and C atoms were confirmed by the peak at 208 (denoted by an asterisk *).[43]

XRD and XPS analysis. According to L. A. Naslund the MAX phase consists of 2D layers of Ti_3C_2 and Al. Ti and C is bonded

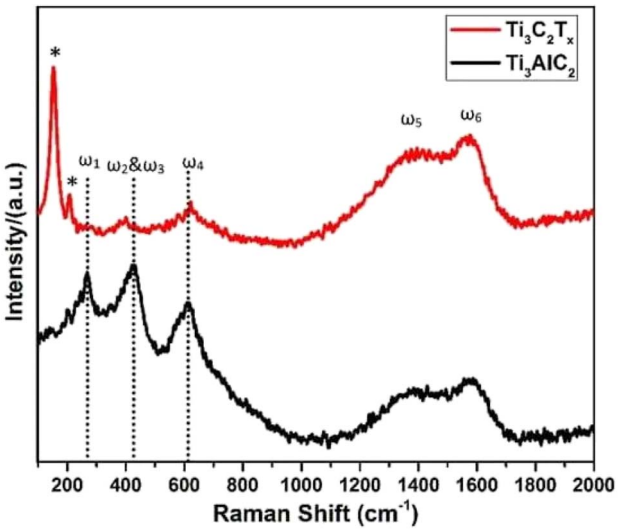

Fig. 5 The Raman spectra exhibit distinctive features for both Ti_3AlC_2 MAX powder and $Ti_3C_2T_x$ MXene. Peaks labeled with "*" specifically correspond to the out-of-plane vibrations of titanium (Ti) and carbon (C) atoms in the structure.

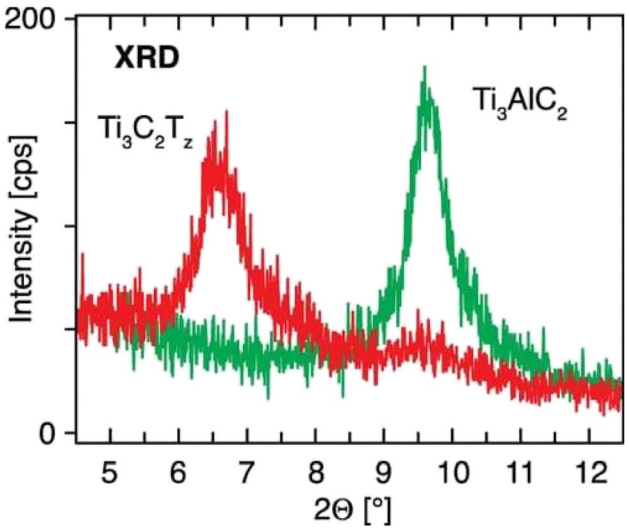

Fig. 7 XRD image of Ti_3AlC_2 and $Ti_3C_2T_x$. The diffractogram shows the Ti_3AlC_2 film at 9.65 and the $Ti_3C_2T_x$ film at 6.60.[45]

via strong covalent bond. Each Ti–C layer is separated by weekly interacting Al layer (Fig. 6).[44]

This X-ray photoelectron spectroscopy data shows us the weak interaction between Ti_3C_2 layers and Al layers, as shown in Fig. 7. This result confirms us also the selective etching of Al layers in MXenes. The sample was prepared by immersion of DC-MS obtained $Ti_3C_2T_x$ in 10% concentrated HF (aq.) for 1 h at room temperature and then rinsing with DI water and ethanol.

Fig. 7 shows the XRD spectrum of Ti_3AlC_2 film at 9.65 and $Ti_3C_2T_x$ film at 6.60, respectively. From this we can confirm that the Al layer is etched from MAX successfully.

Electron energy loss spectroscopy (EELS)

XPS typically provides limited spatial resolution. Therefore, when combined with scanning transmission electron microscopy (STEM), electron energy loss spectroscopy (EELS)[46] becomes a crucial core-level spectroscopic technique that delivers highly detailed spatial information.[47,48] This technique employs a sub-nanometer electron beam probe, ensuring exceptional spatial resolution. As a result, EELS can offer precise chemical bond data on the nanoscale, enabling the characterization of atomic-level bonding environments, such as those found in Ti vacancies and atomic layers within MXene monolayer sheets. In Fig. 8, representative EELS spectra for various edges like C-K, Ti $M_{2,3}$, F-K, and O-K in MXenes are displayed. These spectra facilitate comparisons between selective etching methods utilizing different etching media, such as HF and LiF/HCl.[49] Moreover, EELS opens up opportunities for comprehending chemical reactions at the single-atom level,[50] especially when combined with other imaging and spectral techniques like STEM[51] and energy dispersive X-ray spectroscopy (EDX).[52] This integrated approach enables the identification of Ti adatoms and vacancies within MXene monolayer sheets.

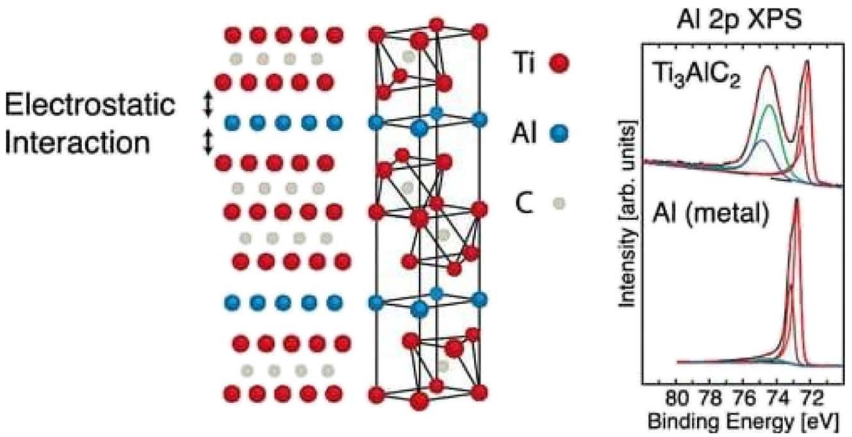

Fig. 6 X-ray photoelectron spectroscopy of Ti_3AlC_2.[45]

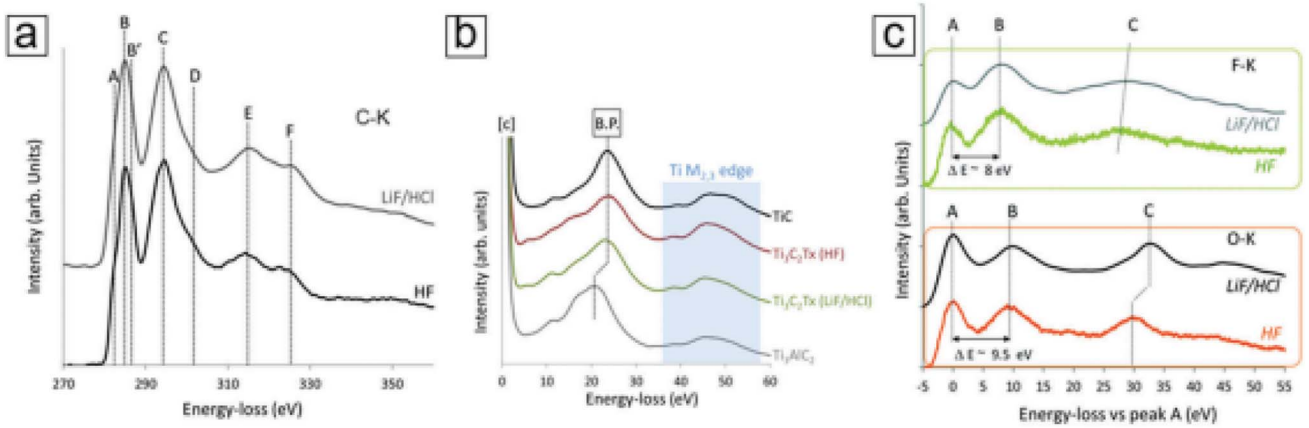

Fig. 8 MXene $Ti_3C_2T_x$ electron energy loss spectroscopy (EELS) curves. (a) C-K edge data of MXenes selectively etched with HF and LiF/HCl. The four major peaks are denoted by the letters C, D, E, and F. (b) The MXenes, TiC, and MAX phases' Ti $M_{2,3}$ edge peaks. The bulk plasmon (shown as B.P. in the figure panel) shifts as a result of exfoliation. (c) MXenes with distinctive peaks at B: 535 eV and 685 eV, respectively, and F-K and O-K edge peaks. By making the first peak (A) in both spectra zero, they both use relative values (copyright 2018 RSC).[53]

SEM analysis. Sometimes oxidation cannot be observed with XRD due to small size or small amount. The structure of MXenes is visualized using scanning electron microscopy (SEM); however, not all etched samples have the same appearance. The "accordion" structure gradually fades away as the HF concentration drops, and the multilayer MXene more closely

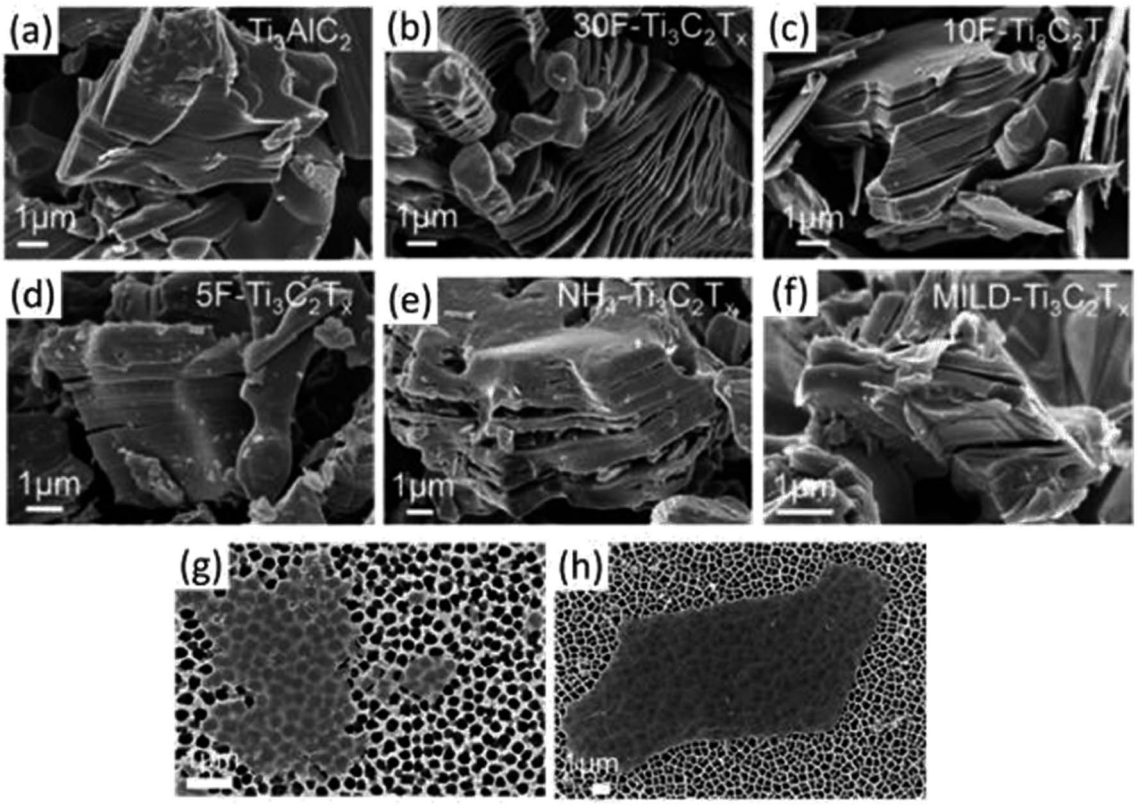

Fig. 9 SEM photos of MXenes and MAX powders created by etching under various circumstances. SEM images of (a) Ti_3AlC_2 (MAX) powder demonstrating the compact layered structure and (b) 30 wt%, (c) 10 wt%, and (d) 5 wt% HF-synthesized multilayered $Ti_3C_2T_x$ powder. Only after etching in (b) 30 wt% HF (or greater HF concentrations) was an accordion-like morphology seen. (e) Ammonium hydrogen fluoride-synthesized multilayered NH_4–$Ti_3C_2T_x$ powder and (f) the MILD technique (etched with LiF in HCl), both of which exhibit negligible opening of MXene lamellas comparable to that seen in 5F $Ti_3C_2T_x$. (g and h) Single MXene flakes on a porous alumina substrate, etched with the 5% HF and MILD methods, are shown in SEM pictures, respectively.[1]

approaches the normal MAX structure. On the outsides of the layers, SEM also exposes oxide nanoparticles, which are a sign of oxidation on the surface and a severe etching process. Fig. 9 shows the SEM images of the MAX phase (a), and multilayered $Ti_3C_2T_x$ powder made with (b) 30 weight percent, (c) 10 weight percent, and (d) 5 weight percent HF as well as compact layered Ti_3AlC_2 (MAX) powder. Only after etching in (b) 30 wt% HF (or greater HF concentrations) was an accordion-like morphology seen. Ammonium hydrogen fluoride-synthesized multilayered NH_4–$Ti_3C_2T_x$ powder (e) and the MILD technique (etched with LiF in HCl) (f) both exhibit negligible opening of MXene lamellas, comparable to that seen in 5F $Ti_3C_2T_x$. SEM pictures of individual MXene flakes etched with the 5 wt% HF and MILD methods, respectively, on a porous alumina substrate are also shown (g and h).

TEM analysis. Fig. 10a demonstrates how MXenes are formed as a thin foil with low magnification. The cross section of exfoliated layers is shown in Fig. 10b, and from this, we may estimate the typical separation. We may obtain the atomistic model of two neighboring Ti_3C_2 molecules from Fig. 10c and d. We may gain a general notion of the *d* spacing of the hexagonal structure of Ti_4C_3 MXene from Fig. 10e and f.

Analysis of the surface chemistry of MXenes is a crucial yet difficult undertaking. It is important to keep in mind that each technique has its own limits while investigating the intricate MXene surface chemistry. For instance, high vacuum conditions are used for EELS and XPS studies. This may cause some of the surface species to desorb. In addition, XPS is a surface method with a penetration depth of 10 nm or less. Raman spectroscopy, in contrast, is not only carried out at ambient circumstances but also makes it simple to conduct *in situ* studies because of the spectrometer's shape. The limited Raman scattering cross-section of metallic materials, however, is known to make them poor Raman scatterers. Additionally, as previously mentioned, MXene peaks are broad, and the spectra can be affected by a variety of circumstances.

Although the majority of the elements (H, C, Al, Si, F, and Li) may be detected *via* NMR analysis, not all of the components present in MXene samples can be. For NMR investigation,[55] the metallic conductivity of MXenes poses new difficulties. Additionally, it's crucial to use water-free samples while performing solid-state NMR on MXenes to prevent signal interference from bulk water. For this reason, annealed samples are used in NMR investigations (200 °C is about right).

Certainly, a comparison chart can provide a concise overview of MXenes in relation to other materials. Below is a simplified comparison chart highlighting the key characteristics of MXenes compared to graphene and traditional semiconductors (*e.g.*, silicon), shown in Table 1. Keep in mind that the actual properties may vary based on specific formulations, synthesis methods, and applications.

Properties

Mechanical properties of MXenes. Bai *et al.* and Magnuson *et al.* found that the surface terminations of MXenes have a stronger interaction between the Ti–O atoms than in the F or OH terminated MXenes and that the Ti–C bond is longer in Ti_2C–T_x than in Ti_2C–T_x. O-terminated MXenes, according to Zha *et al.*, should be the preferred option for applications due to their higher mechanical strength. Chakraborty *et al.* showed that boron-doped Ti_2CO_2 exhibits higher critical strain due to a weaker Ti–C bond. Yorulmaz *et al.* noted that the MXene gets

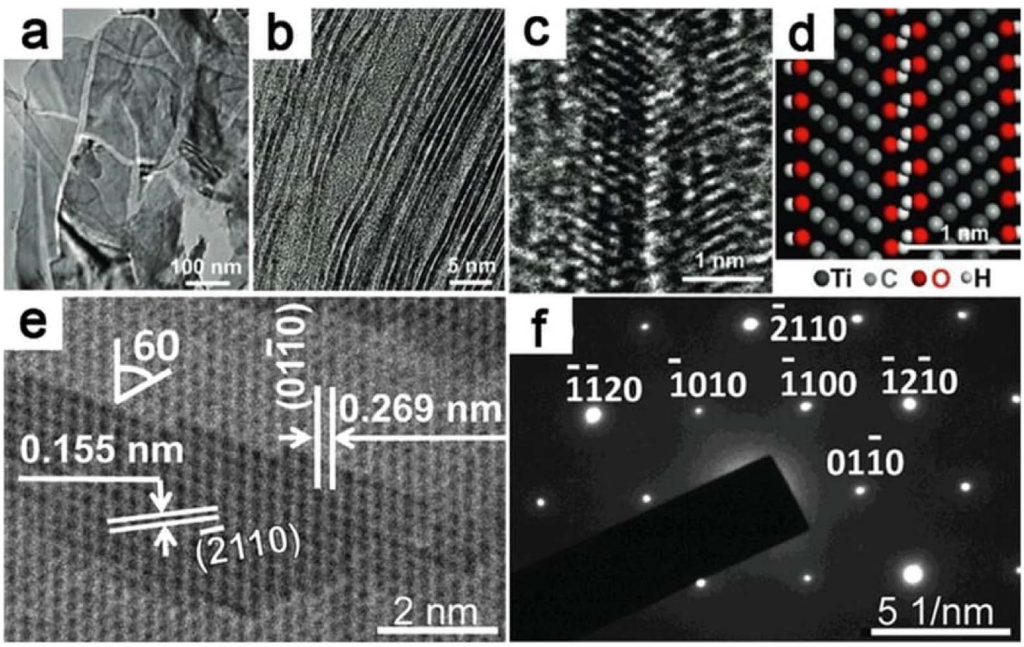

Fig. 10 SAED and TEM imaging of MXenes. (a) A TEM picture of exfoliated Ti–C–O–F 2D nanosheets. (b) MXene sheets with one or two layers. (c) HRTEM picture of bilayer $Ti_3C_2(OH)_xF_y$ (d) its atomistic model of the layer structure (e) HRTEM image of multilayered MXene and (f) MXene's SAED pattern.[54]

Table 1 A comparison chart highlighting the key characteristics of MXenes compared to graphene and silicon

Characteristic	MXene	Graphene	Silicon (Si)
Structure	2D transition metal carbides/nitrides[36]	Single layer of carbon atoms in a hexagonal lattice[56]	Crystalline structure with a diamond-like lattice[57]
Synthesis	Various methods, often involving selective etching[27]	Chemical vapor deposition (CVD), liquid-phase exfoliation[58]	High-temperature purification from silica[59]
Conductivity	Good electrical conductivity[60]	Excellent electrical conductivity[61]	Intrinsic semiconductor with moderate electrical conductivity[62–64]
Mechanical strength	Generally strong, good mechanical properties[65]	Exceptionally strong with high tensile strength[66]	Brittle with lower tensile strength compared to carbon materials[67]
Flexibility	Exhibits flexibility due to its 2D nature[68]	Highly flexible and can be bent without breaking[69]	Rigid crystalline structure, limited flexibility[70]
Optical properties	Variable depending on specific MXene formulation[71]	Transparent and absorbs only ~2.3% of light[72]	Transparent to infrared and visible light[73]
Chemical stability	Stable in various chemical environments[74]	Stable in most environments[75]	Susceptible to oxidation and chemical reactions[76]
Thermal conductivity	Generally high thermal conductivity[77]	High thermal conductivity[78]	Moderate thermal conductivity[79]
Band gap	Tunable band gap (semiconducting behavior)[80]	Zero band gap (semimetallic behavior)[81]	Intrinsic semiconductor with a fixed band gap[82]
Applications	Energy storage, catalysis, sensors, electronics[83,84]	Flexible electronics, sensors, transparent conductive films[85]	Integrated circuits, solar cells, microelectronic[86]
Environmental impact	Depends on synthesis methods, potential concerns[87]	Generally low environmental impact[88]	Energy-intensive production, waste concerns[89]

stiffer as the Young modulus increases. The most important details are that carbide based MXenes are not mechanically stable but are relatively stable in water and dry air.

Structural properties. When MXenes are subjected to high temperatures or metal adsorption processes, surface groups like F, OH, and O can be changed into O terminations.[90] Locations and orientations of surface groups of MXenes are more complicated than expected.

The exact configuration of surface groups of MXenes depends on their synthesis methods. Actually, MXenes will be modeled with terminating species, which is unrealistic.[91] The terminating species that interacted with MXenes with van der Waals or hydrogen bonds should also be taken into account.[92]

Electrical properties. MXenes are known for their high electronic conductivity, which can be increased by cation or organic-molecule intercalation. Zhang *et al.* demonstrated that some OH-terminated MXenes display practically free electron states with a bandgap as large as 0.194 eV, positioned outside the surface atoms and parallel to the surface.[60] It is known that bare MXene species, like $Ti_{n+1}X_n$, exhibit metallic behavior.[93] Due to the formation of more Ti–X bonds, the metallic properties become less strong as n numbers rise.[94] Simply because the N atom has one more electron than the C atom, titanium nitrides have more metallic characteristics than titanium carbides in terms of X atoms. In comparison, depending on the types and orientations of surface groups, terminated MXene sheets can be either narrow-band-gap semiconductors or metals.

Magnetic properties. Although MXenes have powerful and controllable magnetic moments,[95] most of them have non-magnetic ground states as a result of the strong covalent link between the transition metal and the X element.[96] Some bare MXenes, such as Cr_2C and Ti_2N (ferromagnetic),[97,98] Cr_2N, and Mn_2C, are expected to have intrinsic magnetic properties (antiferromagnetic). Surface terminations, flaws in monolayers, and inherent characteristics of the transition metal can all be implicated in magnetism. A new MAX phase with in-plane chemical order was reported in 2017.[99] With Ti atoms as the central layer, double-transition-metal MXenes were investigated and demonstrated how various terminations and cation configurations result in a variety of magnetic orders and properties.[100]

Optical properties. For photovoltaic, photocatalytic, transparent, and optically conducting electrode devices, visible/UV light spectrum absorption is crucial. $Ti_3C_2T_x$ films may capture light energy in the UV-visible range. The spectral range is between 300 and 500 nm.[71] The transmittance of 91% was observed for films as thin as 10 nm. Additionally, depending on the film thickness, it can amass a wide and powerful band of absorption between 700 and 800 nm, which shows the development of light green films and makes it very useful in photothermal therapy applications.[101] Notably, by adjusting its thickness and ion intercalation, the transmittance% could be somewhat optimized. For instance, the tetramethyl compound of ammonium increased the transmittance of the $Ti_3C_2T_x$ screen, while urea, hydrazine, and DMSO decreased it. The properties and corresponding applications of MXenes in different fields are expressed in Table 2.

Application in the field effect transistor

MXene FET for Hg^{2+} and Ag^{+} detection. According to Liu *et al.* MXene FET sensors have shown great potential for the detection and analysis of heavy metal ions such as Hg^{2+}. Hg^{2+} is a toxic heavy metal ion that can cause serious environmental

Table 2 The properties and corresponding applications of MXenes

Properties	Application
Electronic	Gas sensors, technical sensors, biosensing, field effect transistor[102–109]
Magnetic	Spintronics and quantum computing[110–113]
Mechanical	Mechanical reinforcing material, polymer composites[102,114]
Optical and photonic	TCO, saturable absorber, mode-locked laser[115–119]
Electromagnetic	Electromagnetic interference shielding[120–122]
Thermoelectric	Thermoelectric electricity production[123–126]
Chemical	Environmental stability, batteries and supercapacitors, other energy storage environmental and water treatment[3,127–134]
Photothermal	Photothermal therapy[135,136]

and health problems if not properly detected and monitored. MXene FET sensors are based on two-dimensional (2D) layered materials that are highly sensitive to changes in the surrounding environment.

Different techniques have been used for Hg^{2+} detection, such as the fluorescence detection technique,[137] Atomic Absorption Spectroscopy (AAS),[138] $Ti_3C_2T_x$-FET,[139] *etc.* Among them detection with the MXene-FET took only 10 s and it detects 5 ppm mercury ion rapidly, which is efficient. The Hg^{2+} absorption energy of MXenes is very high. It is calculated to be −1.298 eV. By compositing a FET with the MXene it can detect Hg^{2+} rapidly even in a high salinity environment. So, it can be used in real water analysis. It can give a strong response in 1 M NaCl. The sensing capability for Hg^{2+} in tap water is very feasible; it took only 10 s as mentioned earlier during this detection. When Hg^{2+} is absorbed in MXenes, Hg^{2+} is reduced to Hg^{+} and interacts with the surface terminal group such as Cl, as shown in Fig. 11a.[139] The SEM images and output characteristics shown in Fig. 11b and c describe the stability of MXenes after 4 days of storage in air medium. From Fig. 11d we see that the MXene shows *n* type semiconducting nature. Chengbin Liu *et al.* provided a $Ti_3C_2T_x$ MXene FET sensing method for Ag^{+} detection that exhibits outstanding sensing performance in terms of quick response (a few seconds), simplicity of use, and good sensitivity and selectivity.[140]

MXenes for high performance FETs. Using a stacked $Ti_2C(OH)_xF_y$ flake as the source electrode from which the carriers are injected, Jiao Xu *et al.* constructed WSe_2 and MoS_2 FET devices,[141] as shown in Fig. 12a, in which the drain side was in contact with the metal and WSe_2 (or MoS_2) was used as the channel of the p-FET (or n-FET). The scanning electron microscope (SEM) image of a $WSe_2/Ti_2C(OH)_xF_y$ FET is depicted in Fig. 12b. The transport properties of the $WSe_2/Ti_2C(OH)_xF_y$ FET and the $MoS_2/Ti_2C(OH)_xF_y$ FET were examined to look into the

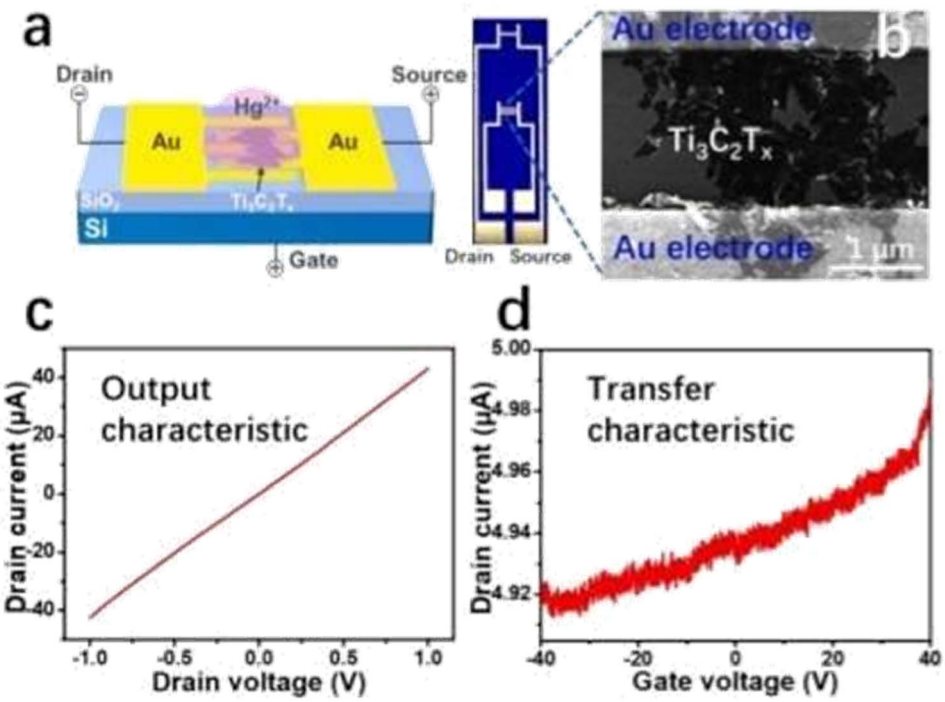

Fig. 11 The $Ti_3C_2T_x$ FET sensor's schematic structure is shown in (a). (b) A picture of the FET sensor electrodes and a SEM image of the $Ti_3C_2T_x$ nanosheets joining the nearby gold finger electrodes. (c) A $Ti_3C_2T_x$ FET device's output characteristics and (d) transfer characteristics.

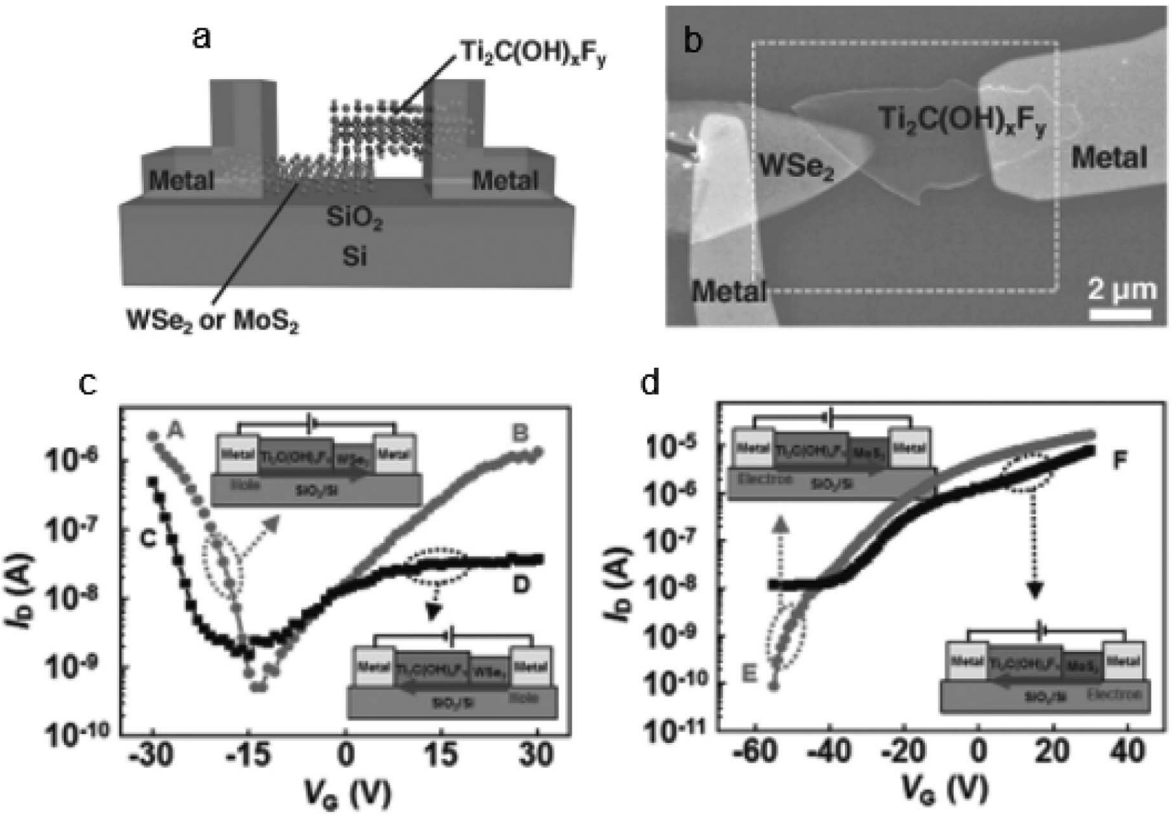

Fig. 12 Schematic of a WSe_2 (or MoS_2)/$Ti_2C(OH)_xF_y$ FET device is shown in (a). (b) Top-view SEM image of a WSe_2/$Ti_2C(OH)_xF_y$ FET. The KPFM mapping zone is shown by the rectangle with a dashed border. (c) I_D–V_G characteristics of the WSe_2/$Ti_2C(OH)_xF_y$ FET. For the negative and positive VDS biases, respectively, there are black squares and circles. The insets display schematic illustrations of how the device works. (d) I_D–V_G properties of the MoS_2/$Ti_2C(OH)_xF_y$ FET. The negative and positive VDS biases are shown, respectively, by the black squares and circles (copyright 2016 John Wiley and Sons).

electronic performance of $Ti_2C(OH)_xF_y$. The I_D–V_G characteristics of a WSe_2/$Ti_2C(OH)_xF_y$ FET tested at room temperature are shown in Fig. 12c. Utilizing the energy band diagrams in Fig. 12d, the MoS_2/$Ti_2C(OH)_xF_y$ FET's transport characteristics were examined.

Hanlin Wang *et al.* showed that the intercalation of $Ti_3C_2T_x$ with didecyldimethyl ammonium bromide (DDAB), a quaternary ammonium chemical, results in a striking improvement in the charge carrier mobility in ambipolar polymer based OFETs.[142] Haihong Xie *et al.* used an MXene ($Ti_3C_2T_x$) as the source electrode and two-dimensional (2D) tin halide perovskite $(PEA)_2SnI_4$ as the semiconductor layer to show how metal halide perovskite field-effect transistors are made.[143] An ultrathin field-effect transistor made of Ti_2CO_2 semiconductor and seamlessly connected Ti_2CF_2 metallic electrodes was considered by Ü. Ö. Akkuş.[144]

For use in high-performance OFETs, Benzheng Lyu *et al.* showed how to fabricate a broad, uniform MXene electrode array on a flexible plastic substrate.[145] They used asymmetric source and drain electrodes to examine the contact characteristics between the MXene electrodes and the organic semiconductors, as illustrated in Fig. 13a. The transfer curves of the p-type pentacene OFETs with varied electrodes are shown in Fig. 13b. Pentacene was injected with holes when negative V_D was supplied to the metal (Au or Al) electrode. Fig. 13b's right panel displays schematic band diagrams of the MXene/pentacene/Au junction at various voltage levels to clarify the carrier injection barrier in each situation.

MXene FET for virus detection. The COVID-19 pandemic infected more than 46.6 M people and 1.2 M deaths occurred worldwide. In October 2020, the total number of cases is 9 M in the US alone.[146] Yanxiao *et al.* fabricated and characterized the 2019-nCoV and influenza virus sensing MXene–graphene field-effect transistor (FET) sensor.[17] An ultra-sensitive virus-sensing transduction material (VSTM) was created by fusing the continuity of large-area high-quality graphene with the high chemical sensitivity of the MXene. The sensor was tested using antigens from two different viruses at different concentrations, and it had an average reaction time of 50 ms and a low limit of detection of 125 copies per mL. The ultra-sensitivity of the sensor was proved by the high signal-to-viral load ratio (10% change in source-drain current and gate voltage). Impedance and field-effect transistor (FET) techniques are frequently used to transmit electrochemical signals. The FET method is perfect for viral sensing because it can accept the 2D VSTM film with ease and generate an electronic output, as shown in Fig. 14.

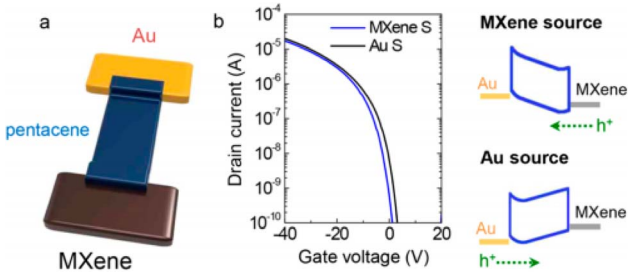

Fig. 13 (a) A schematic depiction of MXene/pentacene/Au. (b) P-type pentacene OFET transfer characteristics with a Au source electrode (black) and MXene source electrode (blue) are shown.[145]

A field-effect transistor (FET)-based biosensing device for detecting SARS-CoV-2 in clinical samples was disclosed by Giwan Seo *et al.*[146] The FET's graphene sheets were coated with an antibody intended to neutralize the SARS-CoV-2 spike protein to develop the sensor. The sensor's performance was evaluated using COVID-19 patients' nasopharyngeal swab samples, cultured virus, and antigen protein (Fig. 15).

MXene FET for salinity estimation. $Ti_3C_2T_x$ showed a high response to detecting high salinity alkalis. So, it can be used in alkali detection in seawater and wastewater. When treated with an alkali there are several changes in $Ti_3C_2T_x$ structure from which we can ensure the detection. Before adding NaOH, C 1s, Ti 2p and oxygen 1s spectra show typical bonds of Ti, C, X, and oxygen.[117,147,148] After adding the alkali, an increase in Ti–OH bond and O–Ti–O bond intensities and a decrease in the intensities of Ti–X bonds are observed.[149]

MXene FETs for chemical sensors. MXenes have demonstrated remarkable electrochemical characteristics. They show significant promise for applications in chemo-resistive gas analysis. Their sensing applications, however, still struggle with low sensitivity and specificity. Among the many difficulties are delayed responsiveness and poor stability. In this article, a unique synthetic method is described for producing $Ti_3C_2T_x$ MXene nanosheets with single-atom Pt (Pt SA) implanted as the sensing channel in field-effect transistor (FET) gas sensors depicted in Fig. 16. This ground-breaking investigation into single-atom catalysts placed on MXene nanosheets for gas detection shows how Pt SA can significantly improve the sensing capabilities of pure $Ti_3C_2T_x$. Triethylamine (TEA) is detected at ppb levels by the Pt SA–$Ti_3C_2T_x$ sensor with a low detection limit of 14 ppb and good multicycle sensing performance. Additionally, the simulation of density functional theory (DFT) and the mechanism of sensor was investigated.[150]

Bingzhe Xu *et al.* created a quick and efficient method for creating FETs based on extremely thin, conductive Ti_3C_2 MXene micropatterns, which were then used to monitor the spiking activity of hippocampus neurons and perform highly sensitive label-free dopamine detection.[151] They used scanning electron microscopy (SEM) to confirm the multilayered structure of the resulting bulk MXenes ($Ti_3C_2T_x$) (Fig. 17a). The chemical makeup of the synthesized MXene was further examined using X-ray diffraction (XRD), which revealed the transition from Ti_3AlC_2 to $Ti_3C_2T_x$ (Fig. 17b). After etching, the Ti_3AlC_2 peak at 39° that was the sharpest vanished, suggesting that the Al layer had been removed. Furthermore, the (00*l*) peaks of $Ti_3C_2T_x$ like (002) at 9.5° and (004) at 19.4° expanded with less intensity and shifted to lower angles, respectively (8.8° and 18.5°), indicating that Al was substituted by OH or F moieties. Few and single layer MXene flakes are prepared for patterning and sensing applications after being delaminated using sonication and intercalated in dimethyl sulfoxide (DMSO) (Fig. 17c).

MXenes as the gate electrode in FETs. MXenes can be employed as the van der Waals gate contact in a GaN high electron mobility transistor (HEMT), according to Chuanju Wang *et al.* The MXene sheets were lift-off constructed as gate electrodes after being spray-coated on AlGaN/GaN epitaxial

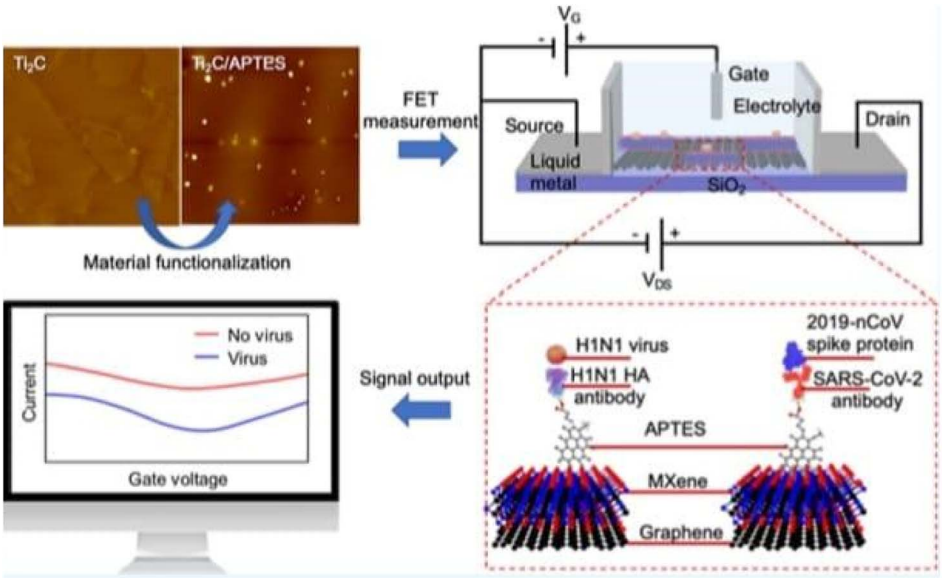

Fig. 14 FET circuit and illustration of the antibody–antigen sensing mechanism and change in drain source current.[17]

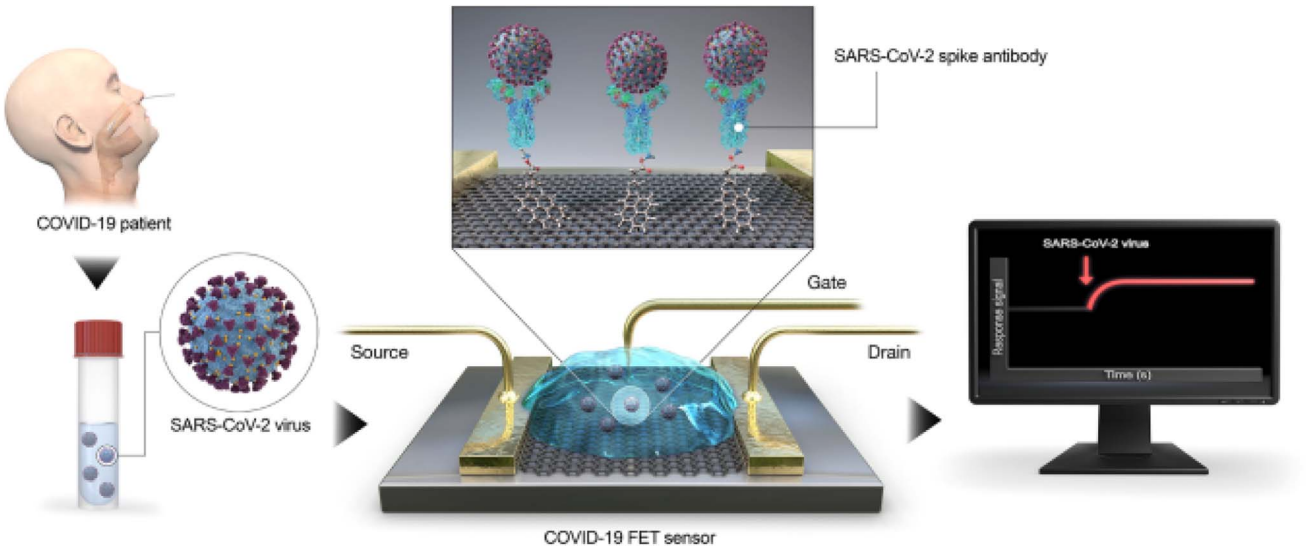

Fig. 15 Diagram showing the steps in the COVID-19 FET sensor functioning. The SARS-CoV-2 spike antibody is attached onto the graphene sheet using the interface molecule 1-pyrenebutyric acid *N*-hydroxysuccinimide ester as a probe linker. Graphene is used as the sensing material.[146]

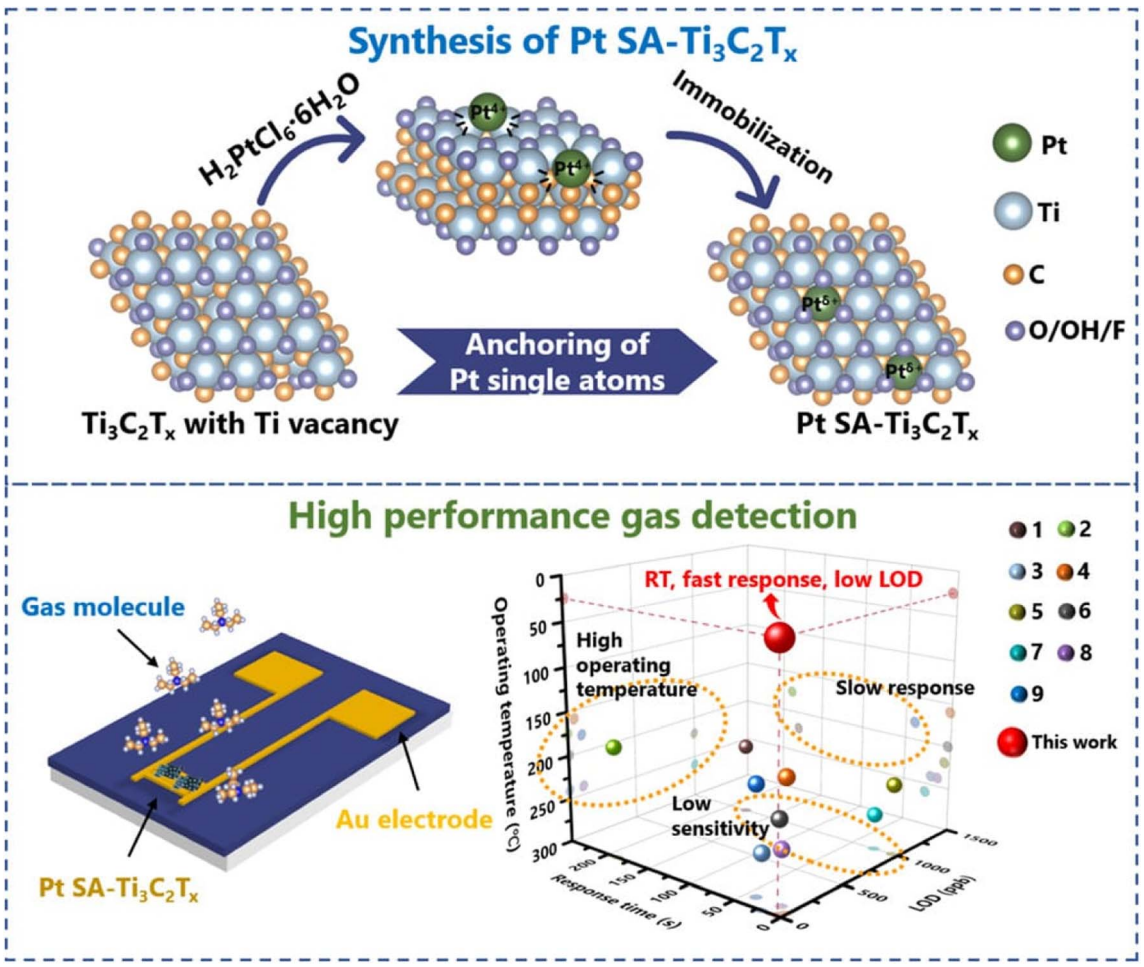

Fig. 16 Schematic diagram of the Pt SA–$Ti_3C_2T_x$ synthesis process and its high detection performance for TEA gas analysis. The Pt SA is synthesized through the immobilization of Pt^{4+} onto the $Ti_3C_2T_x$ surface with Ti vacancies. Schematic diagram of the FET sensor device and the detection performance comparison between Pt SA–$Ti_3C_2T_x$ and other TEA sensors. Data points in the 3D chart are from (1) Pt/SnO_2, (2) Ag/WO_3, (3) Pt SA/WO_3, (4) Fe_2O_3, (5) WO_3/SnO_2, (6) Pd/In_2O_3, (7) Fe/NiO, (8) WO_3/Co_3O_4, and (9) Pt–Ce/In_2O_3.

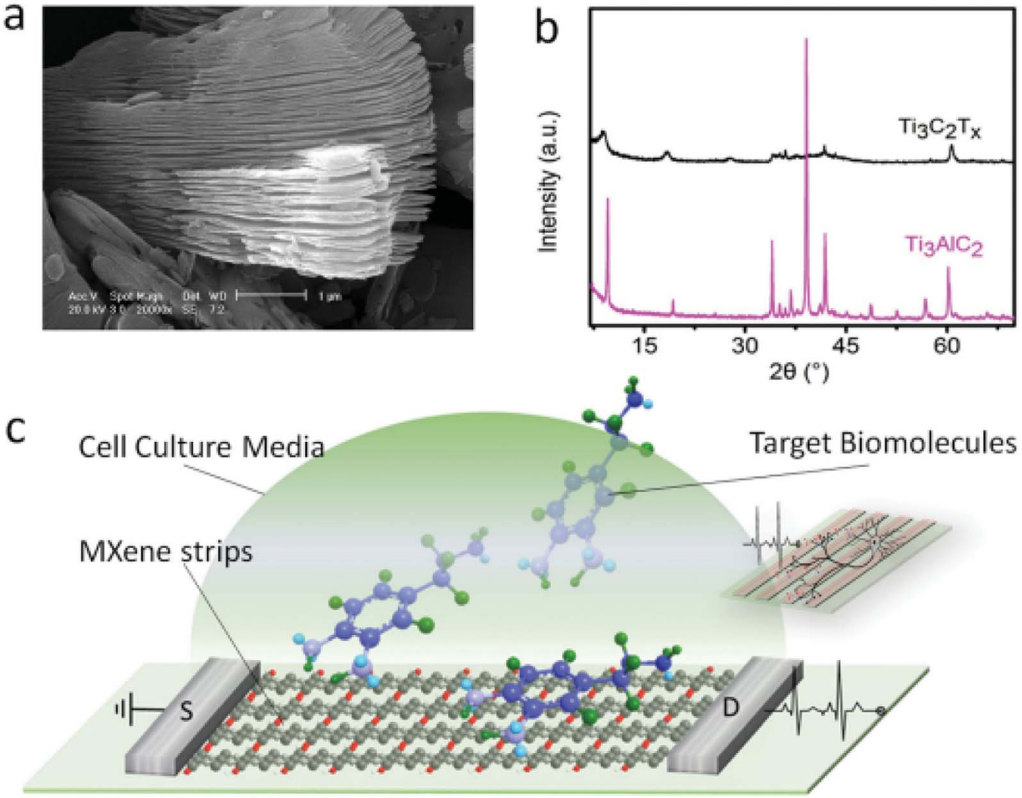

Fig. 17 Characterization of bulk MXenes. (a) SEM image of the multilayer structured MXene. (b) XRD patterns of the transition from Ti_3AlC_2 to $Ti_3C_2T_x$. (c) Schematic of a biosensing device based on MXene field effect transistors (copyright 2016 John Wiley and Sons).[151]

wafers.[152] The scanning transmission electron microscopy (STEM) image was used to calculate the thickness of the $Ti_3C_2T_x$ MXene gate contact, which was found to be 100 nm. Fig. 18a and b demonstrate, respectively, a systematic representation of FET structures before and after the MXene is utilized as the gate. The electron flow path is also displayed underneath the gate. Fig. 18c displays the I_G and logarithmic-scale transfer curves of the GaN HEMTs. Fig. 18d also displays the linear-scale dual-sweep transfer curves for the Ni/Au- and MXene gate GaN HEMTs. Superior interface contact quality is attained thanks to the vdW gap that is created between the MXene films and the AlGaN layer. As a result, during the up-sweep and down-sweep measurements, the MXene-gate GaN HEMTs show a noticeably reduced hysteresis.

MXene FET for exosome detection in human serum. The biomolecules that cancer cells produce, known as exosomes, have great promise for use in clinical diagnostics. Among these, the protein known as cluster of differentiation 9 (CD9) is a significant exosomal biomarker that can be applied to the identification of exosomes. In order to raise the prospect of identifying exosomes in a clinical setting, an extended-gate field-effect transistor (EGFET)-type biosensor with a disposable sensing membrane was first equipped with a CD9 aptamer. Jeongyun An *et al.* detailed the exosome detection using a FET with the help of the MXene with a LOD of 10.64 pM.[153] According to their research, the aptasensor that has been suggested may be an effective instrument for an easy-to-use and quick exosome diagnostic.

MXene FET for IL-6 determination in patients. It was suggested to use spiral interdigitated MXene-assisted field effect transistors (SiMFETs) to measure IL-6 in kidney transplant infection patients by Dawei Li *et al.*[154] Their SiMFETs' improved IL-6 detection range of 10 fg mL^{-1}–100 ng mL^{-1} was made possible by the combination of semiconducting nanocomposites and an upgraded transistor structure. Specifically, the multiple spiral structure of the interdigitated drain-source design enhanced the transconductance of the FET biosensor, while the MXene-based field effect transistor significantly increased the amperometric signal for the detection of IL-6. The SiMFET biosensor that was constructed exhibited acceptable selectivity and repeatability against various biological interferences, along with satisfactory stability for a period of two months. This may pave an alternative strategy for transistor-based biosensors in point-of-care clinical applications.

MXene based FETs have now been used in many other applications like gas sensors,[155] electrochemical transistors,[156] metal halide perovskite vertical FETs,[143] graphene–MXene based materials for diagnosis,[157] *etc.*

Challenges for practical application. The practical application of MXenes in Field Effect Transistors (FETs) presents several challenges that researchers and engineers must overcome for successful implementation. MXene synthesis methods

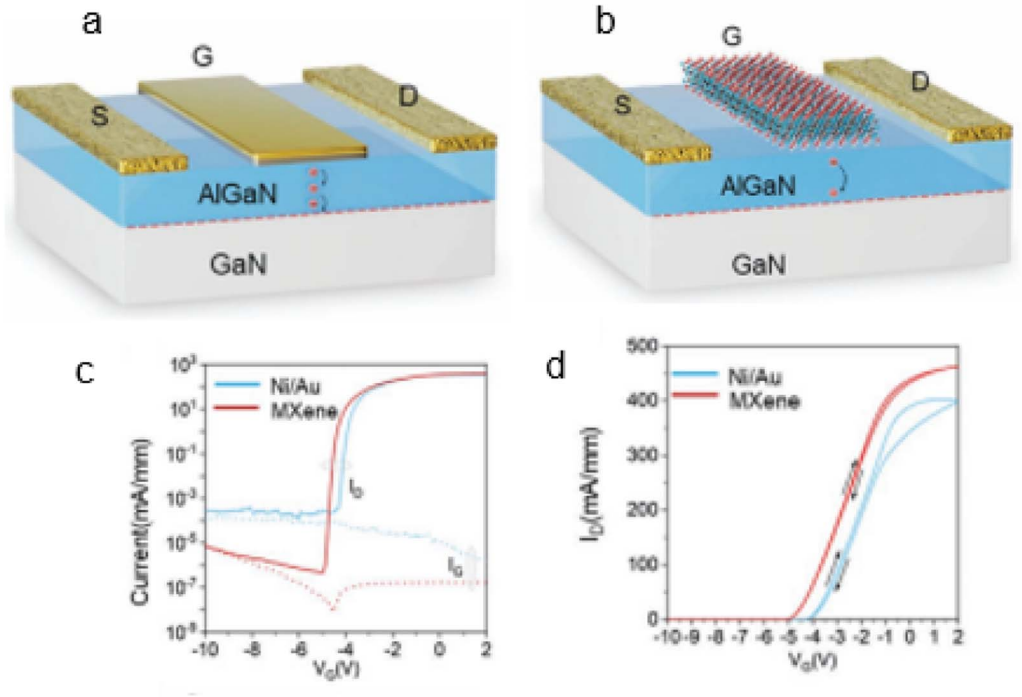

Fig. 18 GaN HEMT schematic diagrams with either $Ti_3C_2T_x$ or (a) Ni/Au or (b) the gate electrodes. (c) The Ni/Au- and MXene-gate GaN HEMTs' I_G curves and logarithmic-scale transfer curves. (d) GaN HEMT dual-sweep transfer curves on a linear scale (copyright 2023 John Wiley and Sons).

need to be optimized for scalability and cost-effectiveness to meet industrial demands. Additionally, achieving consistent quality across large-scale production remains a challenge. MXene materials may exhibit sensitivity to environmental factors such as humidity, temperature, and exposure to certain gases. Ensuring stability under varying conditions is crucial for practical applications in FETs. Achieving low contact resistance between MXenes and electrodes is a common challenge in FETs. High contact resistance can limit device performance, affecting signal integrity and response times. MXene-based FETs may face challenges related to charge carrier mobility. Improving the mobility of charge carriers within the material is essential for achieving high-performance transistors. The dielectric properties of MXenes are critical for FET applications. Ensuring a high-quality dielectric layer is challenging and optimizing dielectric constants for specific FET designs is an ongoing area of research. Integrating MXene-based FETs with existing semiconductor technologies and fabrication processes poses challenges. Compatibility with standard processes and materials used in semiconductor industry practices is crucial for practical adoption. Understanding the long-term stability and reliability of MXene-based FETs is essential for applications requiring extended operational lifetimes. Investigating material degradation and device performance over time is critical for real-world use. Ensuring the purity of MXene materials is vital for consistent performance. Contaminants or impurities during synthesis can affect the electronic properties of MXenes and, consequently, the reliability of FETs. Achieving uniformity and consistency in MXene films or layers is challenging. Variability in thickness or composition can lead to performance variations among devices, impacting reproducibility and reliability. The cost of MXene production and fabrication processes needs to be competitive with existing materials for widespread adoption. Researchers must explore cost-effective synthesis methods and fabrication techniques. Assessing the environmental impact of MXene synthesis and disposal is crucial. Understanding potential environmental risks and developing sustainable practices is essential for the responsible use of MXenes in FET applications.

Addressing these challenges will require collaborative efforts from researchers in materials science, chemistry, and electronics. Overcoming these hurdles will pave the way for the successful integration of MXene-based FETs into practical applications, unlocking the full potential of this promising material in electronic devices.

Conclusion

As we delve deeper into the multifaceted world of MXenes, it becomes increasingly evident that these materials hold the promise of shaping the future of electronic technology. Their unique combination of synthesis versatility, functionalization flexibility, intrinsic properties, and applicability in FETs positions them as a transformative force in the realm of materials science and electronic engineering. This paper will help the researchers to explore the exciting future prospects of MXenes, where their impact on electronic devices is poised to be profound and far-reaching. However, there is still much to be explored in the properties and surface functionalization of MXenes to unlock their full potential. Further work should be

needed for optimizing the doping techniques, understanding the doping mechanism for making more active cites that is useful for any detection and enhance the properties of charge transfer method. And also exploring new application in energy storage ability, flexible circuits sensors and comfortable electronics should be investigated. The unique properties and potential applications of MXenes make them an exciting area of research with the potential to revolutionize various fields of science and technology.

Author contributions

Maisha Rahman: writings, editing; Muhammad Shamim Al Mamun: conceptualization, supervision, writings, and resources.

Conflicts of interest

Authors declare no conflict of interest.

Acknowledgements

Authors love to acknowledge Chemistry Discipline, Khulna University for the technical support.

References

1 Y. Gogotsi and B. Anasori, *ACS Nano*, 2019, **13**, 8491–8494.
2 S. He, X. Sun, H. Zhang, C. Yuan, Y. Wei and J. Li, *Macromol. Rapid Commun.*, 2021, **42**, e2100324.
3 J. Nan, X. Guo, J. Xiao, X. Li, W. Chen, W. Wu, H. Liu, Y. Wang, M. Wu and G. Wang, *Small*, 2021, **17**, e1902085.
4 R. M. Ronchi, J. T. Arantes and S. F. Santos, *Ceram. Int.*, 2019, **45**, 18167–18188.
5 Q. Zhu, J. Li, P. Simon and B. Xu, *Energy Storage Mater.*, 2021, **35**, 630–660.
6 V. Q. Hieu, T. C. Lam, A. Khan, T.-T. Thi Vo, T.-Q. Nguyen, V. D. Doan, D. L. Tran, V. T. Le and V. A. Tran, *Chemosphere*, 2021, **285**, 131429.
7 H. Riazi, M. Anayee, K. Hantanasirisakul, A. A. Shamsabadi, B. Anasori, Y. Gogotsi and M. Soroush, *Adv. Mater. Interfaces*, 2020, **7**, 1902008.
8 K. S. Ranjith, A. T. Ezhil Vilian, S. M. Ghoreishian, R. Umapathi, S.-K. Hwang, C. W. Oh, Y. S. Huh and Y.-K. Han, *J. Hazard. Mater.*, 2022, **421**, 126775.
9 M. Naguib, O. Mashtalir, J. Carle, V. Presser, J. Lu, L. Hultman, Y. Gogotsi and M. W. Barsoum, *ACS Nano*, 2012, **6**, 1322–1331.
10 M. Mozafari and M. Soroush, *Mater. Adv.*, 2021, **2**, 7277–7307.
11 M. Naguib, V. N. Mochalin, M. W. Barsoum and Y. Gogotsi, *Adv. Mater.*, 2014, **26**, 992–1005.
12 M. W. Barsoum, in *MAX Phases*, 2013, pp. 187–235, DOI: 10.1002/9783527654581.ch6.
13 M. Naguib, M. Kurtoglu, V. Presser, J. Lu, J. Niu, M. Heon, L. Hultman, Y. Gogotsi and M. W. Barsoum, *Adv. Mater.*, 2011, **23**, 4248–4253.
14 M. Magnuson, J. Halim and L.-Å. Näslund, *J. Electron Spectrosc. Relat. Phenom.*, 2018, **224**, 27–32.
15 E. N. Hoffman, G. Yushin, T. El-Raghy, Y. Gogotsi and M. W. Barsoum, *Microporous Mesoporous Mater.*, 2008, **112**, 526–532.
16 V. T. Le, Y. Vasseghian, V. D. Doan, T. T. T. Nguyen, T.-T. Thi Vo, H. H. Do, K. B. Vu, Q. H. Vu, T. Dai Lam and V. A. Tran, *Chemosphere*, 2022, **291**, 133025.
17 Y. Li, Z. Peng, N. J. Holl, M. R. Hassan, J. M. Pappas, C. Wei, O. H. Izadi, Y. Wang, X. Dong, C. Wang, Y.-W. Huang, D. Kim and C. Wu, *ACS Omega*, 2021, **6**, 6643–6653.
18 X. Li, G. Fan and C. Zeng, *Int. J. Hydrogen Energy*, 2014, **39**, 14927–14934.
19 B. Hammer and J. K. Nørskov, in *Advances in Catalysis*, Academic Press, 2000, vol. 45, pp. 71–129.
20 Y. Zhang, L. Wang, N. Zhang and Z. Zhou, *RSC Adv.*, 2018, **8**, 19895–19905.
21 N. Chen, W. Yang and C. J. Zhang, *Sci. Technol. Adv. Mater.*, 2021, **22**, 917–930.
22 Z. Wang, *IOP Conf. Ser. Earth Environ. Sci.*, 2021, **714**, 042030.
23 W. Feng, H. Luo, Y. Wang, S. Zeng, Y. Tan, H. Zhang and S. Peng, *Ceram. Int.*, 2018, **44**, 7084–7087.
24 U. U. Rahman, M. Humayun, U. Ghani, M. Usman, H. Ullah, A. Khan, N. M. El-Metwaly and A. Khan, *Molecules*, 2022, **27**(15), 4909–4944.
25 L. Wang, M. Zhang, B. Yang, J. Tan, X. Ding and W. Li, *Small Methods*, 2021, **5**, 2100409.
26 K. R. G. Lim, M. Shekhirev, B. C. Wyatt, B. Anasori, Y. Gogotsi and Z. W. Seh, *Nat. Synth.*, 2022, **1**, 601–614.
27 Y.-J. Kim, S. J. Kim, D. Seo, Y. Chae, M. Anayee, Y. Lee, Y. Gogotsi, C. W. Ahn and H.-T. Jung, *Chem. Mater.*, 2021, **33**, 6346–6355.
28 L. Gao, C. Li, W. Huang, S. Mei, H. Lin, Q. Ou, Y. Zhang, J. Guo, F. Zhang, S. Xu and H. Zhang, *Chem. Mater.*, 2020, **32**, 1703–1747.
29 P. Lakhe, E. M. Prehn, T. Habib, J. L. Lutkenhaus, M. Radovic, M. S. Mannan and M. J. Green, *Ind. Eng. Chem. Res.*, 2019, **58**, 1570–1579.
30 P. Urbankowski, B. Anasori, T. Makaryan, D. Er, S. Kota, P. L. Walsh, M. Zhao, V. B. Shenoy, M. W. Barsoum and Y. Gogotsi, *Nanoscale*, 2016, **8**, 11385–11391.
31 R. S. Alwitt, H. Uchi, T. R. Beck and R. C. Alkire, *Electrochemical Society Extended Abstracts*, 1982, vol. 82-2, pp. 108–109.
32 M. Shen, W. Jiang, K. Liang, S. Zhao, R. Tang, L. Zhang and J. Q. Wang, *Angew Chem. Int. Ed. Engl.*, 2021, **60**, 27013–27018.
33 X. Xiao, H. Song, S. Lin, Y. Zhou, X. Zhan, Z. Hu, Q. Zhang, J. Sun, B. Yang, T. Li, L. Jiao, J. Zhou, J. Tang and Y. Gogotsi, *Nat. Commun.*, 2016, **7**, 11296.
34 W. Weng, B. Jiang, Z. Wang and W. Xiao, *Sci. Adv.*, 2020, **6**, eaay9278.
35 C. Xu, L. Wang, Z. Liu, L. Chen, J. Guo, N. Kang, X.-L. Ma, H.-M. Cheng and W. Ren, *Nat. Mater.*, 2015, **14**, 1135–1141.
36 Y. Gogotsi, *Nat. Mater.*, 2015, **14**, 1079–1080.

37 L. Liu, M. Zhu, Y. Shi, X. Xu, Z. Ma, B. Yu, S. Fu, G. Huang, H. Wang and P. Song, *Chem. Eng. J.*, 2021, **424**, 130338.
38 J. Ji, L. Zhao, Y. Shen, S. Liu and Y. Zhang, *FlatChem*, 2019, **17**, 100128.
39 L. Yin, C. Liu, C. Ding, C. Zhao, I. Z. Mitrovic, E. G. Lim, H. Wang, Y. Sun, Y. Han, Z. Li, L. Yang, C.-Q. Ma and C. Zhao, *Cell Rep. Phys. Sci.*, 2022, **3**, 100905.
40 A. S. R. Bati, A. A. Sutanto, M. Hao, M. Batmunkh, Y. Yamauchi, L. Wang, Y. Wang, M. K. Nazeeruddin and J. G. Shapter, *Cell Rep. Phys. Sci.*, 2021, **2**, 100598.
41 M. Mahmood, A. Rasheed, I. Ayman, T. Rasheed, S. Munir, S. Ajmal, P. O. Agboola, M. F. Warsi and M. Shahid, *Energy Fuels*, 2021, **35**, 3469–3478.
42 E. Satheeshkumar, T. Makaryan, A. Melikyan, H. Minassian, Y. Gogotsi and M. Yoshimura, *Sci. Rep.*, 2016, **6**, 32049.
43 A. Iqbal and N. M. Hamdan, *Materials*, 2021, **14**, 6292–6310.
44 Y. C. Zhou, X. H. Wang, Z. M. Sun and S. Q. Chen, *J. Mater. Chem.*, 2001, **11**, 2335–2339.
45 L.-Å. Näslund, P. O. Å. Persson and J. Rosen, *J. Phys. Chem. C*, 2020, **124**, 27732–27742.
46 C. Wiktor, M. Meledina, S. Turner, O. I. Lebedev and R. A. Fischer, *J. Mater. Chem. A*, 2017, **5**, 14969–14989.
47 S. Carenco, S. Moldovan, L. Roiban, I. Florea, D. Portehault, K. Vallé, P. Belleville, C. Boissière, L. Rozes, N. Mézailles, M. Drillon, C. Sanchez and O. Ersen, *Nanoscale*, 2016, **8**, 1260–1279.
48 R. Pal, A. K. Sikder, K. Saito, A. M. Funston and J. R. Bellare, *Polym. Chem.*, 2017, **8**, 6927–6937.
49 D. Magne, V. Mauchamp, S. Célérier, P. Chartier and T. Cabioc'h, *Phys. Chem. Chem. Phys.*, 2016, **18**, 30946–30953.
50 J. R. Jinschek, *Chem. Commun.*, 2014, **50**, 2696–2706.
51 J. C. Yang, M. W. Small, R. V. Grieshaber and R. G. Nuzzo, *Chem. Soc. Rev.*, 2012, **41**, 8179–8194.
52 L. Zhao, H. Q. Ta, A. Dianat, A. Soni, A. Fediai, W. Yin, T. Gemming, B. Trzebicka, G. Cuniberti, Z. Liu, A. Bachmatiuk and M. H. Rummeli, *Nano Lett.*, 2017, **17**, 4725–4732.
53 J. Pang, R. G. Mendes, A. Bachmatiuk, L. Zhao, H. Q. Ta, T. Gemming, H. Liu, Z. Liu and M. H. Rummeli, *Chem. Soc. Rev.*, 2019, **48**, 72–133.
54 H. Alnoor, A. Elsukova, J. Palisaitis, I. Persson, E. N. Tseng, J. Lu, L. Hultman and P. O. Å. Persson, *Mater. Today Adv.*, 2021, **9**, 100123–100138.
55 T. Kobayashi, Y. Sun, K. Prenger, D.-e. Jiang, M. Naguib and M. Pruski, *J. Phys. Chem. C*, 2020, **124**, 13649–13655.
56 G. Yang, L. Li, W. B. Lee and M. C. Ng, *Sci. Technol. Adv. Mater.*, 2018, **19**, 613–648.
57 T. A. Khachaturova, V. G. But'ko and A. A. Gusev, *JETP Lett.*, 2022, **115**, 41–44.
58 M. Saeed, Y. Alshammari, S. A. Majeed and E. Al-Nasrallah, *Molecules*, 2020, **25**, 3856–3918.
59 A. Daulay, M. Andriayani and S. Gea, *Case Stud. Chem. Environ. Eng.*, 2022, **6**, 100256.
60 N. Zhang, Y. Hong, S. Yazdanparast and M. Asle Zaeem, *2D Mater.*, 2018, **5**, 045004.
61 L. Chen, N. Li, X. Yu, S. Zhang, C. Liu, Y. Song, Z. Li, S. Han, W. Wang, P. Yang, N. Hong, S. Ali and Z. Wang, *Chem. Eng. J.*, 2023, **462**, 142139.
62 M. L. Schultz, *Infrared Phys.*, 1964, **4**, 93–112.
63 K. Huang, Q. Wang, X. Yan, M. Yu, X. Shen, L. Chen and J. Chen, *Opt. Commun.*, 2014, **320**, 169–172.
64 B. O. Kolbesen and A. Mühlbauer, *Solid-State Electron.*, 1982, **25**, 759–775.
65 S. Tian, K. Zhou, C.-Q. Huang, C. Qian, Z. Gao and Y. Liu, *Extreme Mech. Lett.*, 2022, **57**, 101921.
66 D. G. Papageorgiou, I. A. Kinloch and R. J. Young, *Prog. Mater. Sci.*, 2017, **90**, 75–127.
67 M. Ganchenkova and R. M. Nieminen, in *Handbook of Silicon Based MEMS Materials and Technologies*, ed. M. Tilli, T. Motooka, V.-M. Airaksinen, S. Franssila, M. Paulasto-Kröckel and V. Lindroos, William Andrew Publishing, Boston, 2nd edn, 2015, pp. 253–293, DOI: 10.1016/B978-0-323-29965-7.00009-9.
68 Y. Guan, R. Zhao, Y. Cong, K. Chen, J. Wu, H. Zhu, Z. Dong, Q. Zhang, G. Yuan, Y. Li, J. Zhang and X. Li, *Chem. Eng. J.*, 2022, **433**, 133582.
69 U. Stöberl, U. Wurstbauer, W. Wegscheider, D. Weiss and J. Eroms, *Appl. Phys. Lett.*, 2008, **93**, 051906–051909.
70 L. Feng, W. Wang, B. Song, X. Zhu, L. Wang, R. Shao, T. Li, X. Pei, L. Wang, X. Qian and Z. Xu, *Prog. Org. Coat.*, 2023, **174**, 107286.
71 X. Gao, Z. Jia, B. Wang, X. Wu, T. Sun, X. Liu, Q. Chi and G. Wu, *Chem. Eng. J.*, 2021, **419**, 130019.
72 E. D. Obraztsova, M. G. Rybin and P. A. Obraztsov, in *Graphene*, ed. V. Skakalova and A. B. Kaiser, Woodhead Publishing, 2nd edn, 2021, pp. 133–142, DOI: 10.1016/B978-0-08-102848-3.00006-2.
73 M. A. Green and M. J. Keevers, *Prog. Photovolt.: Res. Appl.*, 1995, **3**, 189–192.
74 S. Athavale, S. Micci-Barreca, K. Arole, V. Kotasthane, J. Blivin, H. Cao, J. L. Lutkenhaus, M. Radovic and M. J. Green, *Langmuir*, 2023, **39**, 918–928.
75 S. Lin, J. Tang, K. Zhang, Y. Chen, R. Gao, H. Yin and L.-C. Qin, *Nanoscale Adv.*, 2023, **5**, 1163–1171.
76 L. Duan, D. Walter, N. Chang, J. Bullock, D. Kang, S. P. Phang, K. Weber, T. White, D. Macdonald, K. Catchpole and H. Shen, *Nat. Rev. Mater.*, 2023, **8**, 261–281.
77 C. I. Idumah, *Polym.-Plast. Technol. Mater.*, 2023, **62**, 510–546.
78 D. Kumar Das, H. Bhattacharjee, S. Kumar Sahoo and S. Sahoo, *Mater. Today: Proc.*, 2023, DOI: 10.1016/j.matpr.2023.06.149.
79 C. Cui, Y. Zhang, T. Ouyang, M. Chen, C. Tang, Q. Chen, C. He, J. Li and J. Zhong, *Phys. Rev. Mater.*, 2023, **7**, 033803.
80 C. Hu, Z. Du, Z. Wei, L. Li and G. Shen, *Appl. Phys. Rev.*, 2023, **10**, 021402–021410.
81 A. M. Rojas-Cuervo and R. R. Rey-González, *Chem. Phys.*, 2023, **565**, 111744.
82 P. Saha, S. Majety and M. Radulaski, *Sci. Rep.*, 2023, **13**, 4112.
83 S. Nahirniak, A. Ray and B. Saruhan, *Batteries*, 2023, **9**, 126.

84 Q. Wang, N. Han, Z. Shen, X. Li, Z. Chen, Y. Cao, W. Si, F. Wang, B.-J. Ni and V. K. Thakur, *Nano Mater. Sci.*, 2023, **5**, 39–52.
85 H. Lin, Q. Jian, X. Bai, D. Li, Z. Huang, W. Huang, S. Feng and Z. Cheng, *Appl. Therm. Eng.*, 2023, **218**, 119176.
86 S. P. Muduli and P. Kale, *Mater. Sci. Semicond. Process.*, 2023, **154**, 107202.
87 N. H. Solangi, R. R. Karri, S. A. Mazari, N. M. Mubarak, A. S. Jatoi, G. Malafaia and A. K. Azad, *Coord. Chem. Rev.*, 2023, **477**, 214965.
88 V. Manikandan and N. Y. Lee, *Chemosphere*, 2023, **311**, 136934.
89 H. Liang and F. You, *Nat. Commun.*, 2023, **14**, 1274.
90 X. Xie, S. Chen, W. Ding, Y. Nie and Z. Wei, *Chem. Commun.*, 2013, **49**, 10112–10114.
91 J.-C. Lei, X. Zhang and Z. Zhou, *Front. Phys.*, 2015, **10**, 276–286.
92 X. Wang, X. Shen, Y. Gao, Z. Wang, R. Yu and L. Chen, *J. Am. Chem. Soc.*, 2015, **137**, 2715–2721.
93 M. Kurtoglu, M. Naguib, Y. Gogotsi and M. W. Barsoum, *MRS Commun.*, 2012, **2**, 133–137.
94 H. Lashgari, M. R. Abolhassani, A. Boochani, S. M. Elahi and J. Khodadadi, *Solid State Commun.*, 2014, **195**, 61–69.
95 M. Khazaei, M. Arai, T. Sasaki, C.-Y. Chung, N. S. Venkataramanan, M. Estili, Y. Sakka and Y. Kawazoe, *Adv. Funct. Mater.*, 2013, **23**, 2185–2192.
96 C. Si, J. Zhou and Z. Sun, *ACS Appl. Mater. Interfaces*, 2015, **7**, 17510–17515.
97 G. Gao, G. Ding, J. Li, K. Yao, M. Wu and M. Qian, *Nanoscale*, 2016, **8**, 8986–8994.
98 G. Wang, *J. Phys. Chem. C*, 2016, **120**, 18850–18857.
99 W. Sun, Y. Xie and P. R. C. Kent, *Nanoscale*, 2018, **10**, 11962–11968.
100 Y. Yuan, D. Cao, Y. Zhang, J. Ma, J. Qi, Q. Wang, G. Lu, Y. Wu, J. Yan, Y. Shi, X. Zhang and G. F. Gao, *Nat. Commun.*, 2017, **8**, 15092.
101 K. Rasool, R. P. Pandey, P. A. Rasheed, S. Buczek, Y. Gogotsi and K. A. Mahmoud, *Mater. Today*, 2019, **30**, 80–102.
102 J. L. Hart, K. Hantanasirisakul, A. C. Lang, B. Anasori, D. Pinto, Y. Pivak, J. T. van Omme, S. J. May, Y. Gogotsi and M. L. Taheri, *Nat. Commun.*, 2019, **10**, 522.
103 R. Ibragimova, P. Erhart, P. Rinke and H. P. Komsa, *J. Phys. Chem. Lett.*, 2021, **12**, 2377–2384.
104 R. Bhardwaj and A. Hazra, *J. Mater. Chem. C*, 2021, **9**, 15735–15754.
105 S. J. Kim, H.-J. Koh, C. E. Ren, O. Kwon, K. Maleski, S.-Y. Cho, B. Anasori, C.-K. Kim, Y.-K. Choi, J. Kim, Y. Gogotsi and H.-T. Jung, *ACS Nano*, 2018, **12**, 986–993.
106 J. Choi, Y.-J. Kim, S.-Y. Cho, K. Park, H. Kang, S. J. Kim and H.-T. Jung, *Adv. Funct. Mater.*, 2020, **30**, 2003998.
107 Y.-W. Cai, X.-N. Zhang, G.-G. Wang, G.-Z. Li, D.-Q. Zhao, N. Sun, F. Li, H.-Y. Zhang, J.-C. Han and Y. Yang, *Nano Energy*, 2021, **81**, 105663.
108 K. Chang, M. Guo, L. Pu, J. Dong, L. Li, P. Ma, Y. Huang and T. Liu, *Chem. Eng. J.*, 2023, **451**, 138578.
109 Y. Wang, Y. Yue, F. Cheng, Y. Cheng, B. Ge, N. Liu and Y. Gao, *ACS Nano*, 2022, **16**, 1734–1758.
110 Q. Song, F. Ye, L. Kong, Q. Shen, L. Han, L. Feng, G. Yu, Y. Pan and H. Li, *Adv. Funct. Mater.*, 2020, **30**, 2000475.
111 L. Gao, W. Bao, A. V. Kuklin, S. Mei, H. Zhang and H. Ågren, *Adv. Mater.*, 2021, **33**, e2004129.
112 E. M. D. Siriwardane, P. Karki, Y. L. Loh and D. Çakır, *J. Phys. Chem. C*, 2019, **123**, 12451–12459.
113 Y. Zhang, B. Sa, N. Miao, J. Zhou and Z. Sun, *J. Mater. Chem. A*, 2021, **9**, 10882–10892.
114 R. Thankappan, K. G. Vasanthakumari and U. M. Uzma Sulthana, *J. Mater. Sci.: Mater. Electron.*, 2022, **33**, 24542–24549.
115 G. R. Berdiyorov, *AIP Adv.*, 2016, **6**, 055105–055112.
116 A. Di Vito, A. Pecchia, M. Auf der Maur and A. Di Carlo, *Adv. Funct. Mater.*, 2020, **30**, 1909028.
117 Y. I. Jhon, J. Koo, B. Anasori, M. Seo, J. H. Lee, Y. Gogotsi and Y. M. Jhon, *Adv. Mater.*, 2017, **29**, 1702496.
118 W. Shui, J. Li, H. Wang, Y. Xing, Y. Li, Q. Yang, X. Xiao, Q. Wen and H. Zhang, *Adv. Opt. Mater.*, 2020, **8**, 2001120.
119 L. Gao, C. Ma, S. Wei, A. V. Kuklin, H. Zhang and H. Ågren, *ACS Nano*, 2021, **15**, 954–965.
120 J. Liu, H. B. Zhang, R. Sun, Y. Liu, Z. Liu, A. Zhou and Z. Z. Yu, *Adv. Mater.*, 2017, **29**, 1702367–1702372.
121 M.-S. Cao, Y.-Z. Cai, P. He, J.-C. Shu, W.-Q. Cao and J. Yuan, *Chem. Eng. J.*, 2019, **359**, 1265–1302.
122 Q.-W. Wang, H.-B. Zhang, J. Liu, S. Zhao, X. Xie, L. Liu, R. Yang, N. Koratkar and Z.-Z. Yu, *Adv. Funct. Mater.*, 2019, **29**, 1806819.
123 H. Kim, B. Anasori, Y. Gogotsi and H. N. Alshareef, *Chem. Mater.*, 2017, **29**, 6472–6479.
124 S. Sarikurt, D. Çakır, M. Keçeli and C. Sevik, *Nanoscale*, 2018, **10**, 8859–8868.
125 X. Lu, Q. Zhang, J. Liao, H. Chen, Y. Fan, J. Xing, S. Gu, J. Huang, J. Ma, J. Wang, L. Wang and W. Jiang, *Adv. Energy Mater.*, 2020, **10**, 1902986.
126 W. Ding, P. Liu, Z. Bai, Y. Wang, G. Liu, Q. Jiang, F. Jiang, P. Liu, C. Liu and J. Xu, *Adv. Mater. Interfaces*, 2020, **7**, 2001340.
127 J. Ma, Q. Jiang, Y. Zhou, W. Chu, S. Perathoner, C. Jiang, K. H. Wu, G. Centi and Y. Liu, *Small*, 2021, **17**, e2007509.
128 X. Li, Z. Huang, C. E. Shuck, G. Liang, Y. Gogotsi and C. Zhi, *Nat. Rev. Chem*, 2022, **6**, 389–404.
129 Y. Wei, L. Xiang, H. Ou, F. Li, Y. Zhang, Y. Qian, L. Hao, J. Diao, M. Zhang, P. Zhu, Y. Liu, Y. Kuang and G. Chen, *Adv. Funct. Mater.*, 2020, **30**, 2005135.
130 H. Chen, Y. Wen, Y. Qi, Q. Zhao, L. Qu and C. Li, *Adv. Funct. Mater.*, 2020, **30**, 1906996.
131 J. Yang, W. Bao, P. Jaumaux, S. Zhang, C. Wang and G. Wang, *Adv. Mater. Interfaces*, 2019, **6**, 1802004.
132 K. Li, M. Liang, H. Wang, X. Wang, Y. Huang, J. Coelho, S. Pinilla, Y. Zhang, F. Qi, V. Nicolosi and Y. Xu, *Adv. Funct. Mater.*, 2020, **30**, 2000842.
133 Q. Lin, G. Zeng, G. Yan, J. Luo, X. Cheng, Z. Zhao and H. Li, *Chem. Eng. J.*, 2022, **427**, 131668.
134 L. Liao, D. Jiang, K. Zheng, M. Zhang and J. Liu, *Adv. Funct. Mater.*, 2021, **31**, 2103960.
135 H. Lin, Y. Wang, S. Gao, Y. Chen and J. Shi, *Adv. Mater.*, 2018, **30**, 1703284–1703294.

136 Y. Liu, Q. Han, W. Yang, X. Gan, Y. Yang, K. Xie, L. Xie and Y. Deng, *Mater. Sci. Eng., C*, 2020, **116**, 111212.
137 Y. Li, N. Liu, H. Liu, Y. Wang, Y. Hao, X. Ma, X. Li, Y. Huo, J. Lu, S. Tang, C. Wang, Y. Zhang and Z. Gao, *Sci. Rep.*, 2017, **7**, 45974.
138 H. Erxleben and J. Ruzicka, *Anal. Chem.*, 2005, **77**, 5124–5128.
139 Y. V. Fedoseeva, A. S. Orekhov, G. N. Chekhova, V. O. Koroteev, M. A. Kanygin, B. V. Senkovskiy, A. Chuvilin, D. Pontiroli, M. Riccò, L. G. Bulusheva and A. V. Okotrub, *ACS Nano*, 2017, **11**, 8643–8649.
140 C. Liu, X. Wei, S. Hao, B. Zong, X. Chen, Z. Li and S. Mao, *Anal. Chem.*, 2021, **93**, 8010–8018.
141 J. Xu, J. Shim, J.-H. Park and S. Lee, *Adv. Funct. Mater.*, 2016, **26**, 5328–5334.
142 H. Wang, Y. Wang, Z. Ni, N. Turetta, S. M. Gali, H. Peng, Y. Yao, Y. Chen, I. Janica, D. Beljonne, W. Hu, A. Ciesielski and P. Samori, *Adv. Mater.*, 2021, **33**, e2008215.
143 H. Xie, P.-A. Chen, X. Qiu, Y. Liu, J. Xia, J. Guo, H. Wei, Z. Gong, J. Ding and Y. Hu, *Appl. Phys. Lett.*, 2023, **122**, 153301–153308.
144 Ü. Ö. Akkuş, E. Balcı and S. Berber, *Superlattices Microstruct.*, 2020, **140**, 106433–106438.
145 B. Lyu, M. Kim, H. Jing, J. Kang, C. Qian, S. Lee and J. H. Cho, *ACS Nano*, 2019, **13**, 11392–11400.
146 G. Seo, G. Lee, M. J. Kim, S. H. Baek, M. Choi, K. B. Ku, C. S. Lee, S. Jun, D. Park, H. G. Kim, S. J. Kim, J. O. Lee, B. T. Kim, E. C. Park and S. I. Kim, *ACS Nano*, 2020, **14**, 5135–5142.
147 M. Han, X. Yin, H. Wu, Z. Hou, C. Song, X. Li, L. Zhang and L. Cheng, *ACS Appl. Mater. Interfaces*, 2016, **8**, 21011–21019.
148 X. Chen, X. Sun, W. Xu, G. Pan, D. Zhou, J. Zhu, H. Wang, X. Bai, B. Dong and H. Song, *Nanoscale*, 2018, **10**, 1111–1118.
149 C. Liu, S. Hao, X. Chen, B. Zong and S. Mao, *ACS Appl. Mater. Interfaces*, 2020, **12**, 32970–32978.
150 B. Zong, Q. Xu and S. Mao, *ACS Sens.*, 2022, **7**, 1874–1882.
151 B. Xu, M. Zhu, W. Zhang, X. Zhen, Z. Pei, Q. Xue, C. Zhi and P. Shi, *Adv. Mater.*, 2016, **28**, 3333–3339.
152 C. Wang, X. Xu, S. Tyagi, P. C. Rout, U. Schwingenschlögl, B. Sarkar, V. Khandelwal, X. Liu, L. Gao, M. N. Hedhili, H. N. Alshareef and X. Li, *Adv. Mater.*, 2023, 2211738.
153 J. An, H. Park, J. Kim, H. Park, T.-H. Kim, C. Park, J. Kim, M.-H. Lee and T. Lee, *ACS Sens.*, 2023, **8**, 3174–3186.
154 D. Li, Y. Ren, R. Chen, H. Wu, S. Zhuang and M. Zhang, *Microchim. Acta*, 2023, **190**, 284.
155 P. Baraneedharan, D. Shankari, A. Arulraj, P. J. Sephra, R. V. Mangalaraja and M. Khalid, *J. Electrochem. Soc.*, 2023, **170**, 107501.
156 Y.-C. Zhu, B. Cai, Q. Jiang, Y. Zhang, J. Sha and S. Xie, *J. Nanobiotechnol.*, 2021, **19**, 386.
157 A. Zarepour, Ç. Karasu, Y. Mir, M. H. Nematollahi, S. Iravani and A. Zarrabi, *Biomater. Sci.*, 2023, **11**, 6687–6710.